frontiers | Frontiers in Environmental Archaeology

TYPE Hypothesis and Theory
PUBLISHED 14 September 2023
DOI 10.3389/fearc.2023.1221130

OPEN ACCESS

EDITED BY
Peter Bray,
University of Reading, United Kingdom

REVIEWED BY
Yimin Yang,
University of Chinese Academy of Sciences, China
Alicia Van Ham-Meert,
KU Leuven, Belgium

*CORRESPONDENCE
Adi Eliyahu-Behar
✉ adieli@ariel.ac.il
Naama Yahalom-Mack
✉ Naama.Yahalom@mail.huji.ac.il

†These authors have contributed equally to this work

RECEIVED 11 May 2023
ACCEPTED 03 August 2023
PUBLISHED 14 September 2023

CITATION
Eliyahu-Behar A, Ben Dor Y, Brauns M, Shulman OA, Avni Y, Killebrew AE, Tirosh O and Yahalom-Mack N (2023) "A land whose stones are iron..."—Iron ore sources in the Southern Levant. *Front. Environ. Archaeol.* 2:1221130. doi: 10.3389/fearc.2023.1221130

"A land whose stones are iron..."—Iron ore sources in the Southern Levant

Adi Eliyahu-Behar[1*†], Yoav Ben Dor[2], Michael Brauns[3], Oriana Adi Shulman[4], Yoav Avni[2], Ann E. Killebrew[5], Ofir Tirosh[4] and Naama Yahalom-Mack[6*†]

[1]The Department of Chemical Sciences, Institute of Archaeology, Ariel University, Ari'el, Israel, [2]Geological Survey of Israel, Jerusalem, Israel, [3]Curt-Engelhorn-Zentrum Archaömetrie, Mannheim, Germany, [4]The Fredy and Nadine Institute of Earth Sciences, The Hebrew University of Jerusalem, Jerusalem, Israel, [5]Classics and Ancient Mediterranean Studies, Jewish Studies, and Anthropology, The Pennsylvania State University, University Park, PA, United States, [6]Institute of Archaeology, The Hebrew University of Jerusalem, Jerusalem, Israel

Recent discoveries of iron production remains in multiple Iron Age sites throughout the Southern Levant indicate the significance of iron production in the region during this time. However, one main question remains unanswered—that is, provenance: Where were the iron resources located? Were they local or brought from afar? Answering these questions would allow great potential for reconstructing iron-ore procurement strategies and exploitation practices in the social, political, and economic context of the Southern Levant in the early 1st millennium BCE. It has long been assumed that iron ore, prevalent in the Earth's crust, is widely available. However, since high-grade ore was required for the smelting technology of the time, the bloomery process, only selected iron ore deposits in the region were suitable. This study aims to identify and characterize chemically and isotopically enriched iron-ore sources in the Southern Levant. Samples were collected from sedimentary and hydrothermal sources and analyzed for their iron content, trace elements composition, and osmium (Os) isotopic ratios. Here, we present the results of this preliminary investigation, introducing several substantial ore sources in the region and demonstrating the possibility of differentiating between these sources based on their chemical and Os isotopic composition. Finally, hematite objects from selected Iron Age archaeological sites are compared against the analyzed ore sources, showing inconsistency with the sampled ores.

KEYWORDS

iron ores, bloomery process, iron provenance, osmium isotope analysis, Southern Levant

1. Introduction

Iron is the fourth-most common element in the Earth's crust, forming much of the planet's outer and inner core. It is highly reactive within the environment and thus rare in its metallic state, limited mainly to deposition by meteorites. By contrast, iron-bearing minerals (ores) are among the most abundant in the Earth's crust and are often considered commonly available for exploitation. Nonetheless, compared with other mineral ores exploited in antiquity to produce metals, such as copper, lead, and silver, humans began to master iron-smelting technology in Eurasia only much later, toward the end of the 2nd millennium BCE (Erb-Satullo, 2019). This invention, namely the bloomery process, is commonly considered to be one of the most important and influential technological breakthroughs in human evolution (Tylecote, 1992; Buchwald and Wivel, 1998).

In the Southern Levant, iron gradually appeared during the late 2nd millennium BCE, primarily for prestigious use. Beginning in the 10th century BCE, the situation changed dramatically. Iron was used predominantly for agriculture and warfare, and evidence for iron production has been identified in multiple settlement sites (McNutt, 1990; Bunimovitz and Lederman, 2003; Veldhuijzen and Rehren, 2007; Eliyahu-Behar et al., 2012, 2013; Yahalom-Mack and Eliyahu-Behar, 2015; Killebrew and Quartermaine, 2016; Erb-Satullo and Walton, 2017; Erb-Satullo, 2019). The identification of iron production remains as early as the 10th century BCE indicated that this region was one of the first in the world to adopt iron for systematic tool and weapon production.

Based on the evidence at hand, in particular the location of production venues adjacent to or in association with administrative and public buildings, it had been suggested that the newly emerging political powers of the region were involved in the introduction and assimilation of the new technology (Bunimovitz and Lederman, 2012; Yahalom-Mack et al., 2017; Workman et al., 2020; Killebrew, 2023). With the considerable increase in the number of day-to-day iron artifacts during the mid-10th century BCE (Waldbaum, 1978, 1999; McNutt, 1990; Gottlieb, 2010; Yahalom-Mack and Eliyahu-Behar, 2015; Yahalom-Mack and Rabinovich, 2020), identifying the source of the iron used is most significant for understanding the social, political, and economic implications of the introduction of iron metallurgy into the region. Here, too, iron was considered widespread, an idea that is echoed in Deuteronomy 8:9: "A land whose stones are iron." While this may be true, it remains to be determined how many of the deposits were rich enough to have been smelted using the prevailing technology of the time—the bloomery process—and which ore sources were, in fact, used during the Iron Age.

To date, no systematic attempt has been made to determine the provenance of iron objects from the Iron Age or from the subsequent periods in the Southern Levant. The most common method for establishing provenance, which utilizes slag inclusion analysis, has rarely been implemented, perhaps because of the lack of comparative material and the generally poor preservation of the iron, which is seldom maintained in its metallic form (Eliyahu-Behar and Yahalom-Mack, 2018). In the Southern Levant, only a single ore source, the Mugharet el-Wardeh ore deposit in the Ajlun, Jordan, yielded evidence for iron smelting in its vicinity, at Tell Hammeh (Veldhuijzen and van der Steen, 1999; Veldhuijzen and Rehren, 2007). The site, exhibiting tap-furnace smelting activities, was dated to the late 10th and early 9th centuries BCE based on three radiocarbon dates. An attempt to determine the provenance of iron objects from Tel Beth Shemesh, based on the analysis of slag inclusions, showed inconsistency with the Tell Hammeh (Ajlun) smelting slag (Blakelock et al., 2009). Another attempt to establish provenance, using chemical composition, suggested a correlation between iron objects from Beth Shemesh and the iron-rich nodules from the Adulam formation, which is located in the vicinity of the site (Ilani et al., 2020; and see the following discussion).

While chemical and lead isotope analysis (LIA) are routinely applied to determining the provenance of lead, silver, and copper-based alloys, the applicability of this method to iron and ferrous metals was shown to be impractical due to the generally low content of lead in iron ores and the high inhomogeneity of lead concentrations within ore deposits (Schwab et al., 2006). Os, by comparison, is highly siderophile in nature and hence significant. In a recent study, through a series of experimental iron smelts, using three iron-ore deposits collected from the Negev region (Israel), we produced consolidated blooms, slags, and metal bars, which were analyzed for the development and assessment of the potential of osmium (Os) isotope analysis for determining the provenance of iron (Brauns et al., 2013, 2020). An analysis of the Os isotopic composition of the ores, blooms, and metal bars obtained from these experiments confirmed that the $^{187}Os/^{188}Os$ isotopic ratio is maintained during the transition from ore to metal, with no significant isotopic fractionation, and that an enrichment/depletion of Os content occurred between ore to metal and ore to slag as expected (Brauns et al., 2020: Figure 6; Stepanov et al., 2022; Eliyahu-Behar, 2023).

Provenance methods for iron, whether utilizing slag inclusion analysis, bulk geochemical analysis, or isotope analysis, rely heavily on knowledge of the relevant geological sources. This study presents the first step in identifying and characterizing rich-iron sources in the Southern Levant that could have been used for the production of iron. Utilizing Os and detailed chemical analyses of selected iron ores from the region, we examine the variability between the main ore sources. These results will be useful for future iron provenance studies in the region.

Thirty-five samples were collected from 14 major deposits (Table 1, Figure 1). The samples were characterized for their mineralogical (using X-ray diffraction [XRD] and Fourier-transform infrared spectroscopy [FTIR]), geochemical (using inductively coupled plasma atomic emission spectroscopy [ICP-AES] and laser ablation inductively coupled plasma mass spectrometry [LA-ICP-MS]), and Os isotopic compositions. Although only a few samples were collected at each location, the samples included the rich iron phase (mostly hematite and goethite), with a minor presence of gangue minerals, and can be considered representative.

A second data set analyzed in this study comprised selected hematite artifacts from Early Iron Age settlement strata. These were sampled under the assumption that some may originate from iron sources and may direct us toward them. As these are shaped from the original bulk rock, they are expected to have a similar chemical and isotopic signature if they originated from one of the studied ores.

2. Materials

2.1. Surveyed iron deposits

Iron-ore deposits in the Southern Levant, mainly west of the Jordan River, were thoroughly prospected and mapped during the 1950s by the Geological Survey of Israel. The deposits were categorized as derived from two main types of geological formations: sedimentary and epigenetic hydrothermal deposits (see the following subsections). The former are mostly known in the upper Galilee, for example at Ramim-Manara Ridge, and at the Ramon Crater in Israel's Negev desert but also occur as nodules in other formations, such as the Ora Formation of

10.3389/fearc.2023.1221130

TABLE 1 Surveyed ore deposits, their geological formation, and general description.

Ore body	Sample No.	Geographic region	GPS coordinates		Geological formation/ age	Hosting rock	Description
Ramim–Manara	IP23	Naftali Mountains, Upper Galilee	35.56063	33.201035	Hydra, Lower Cretaceous	Sandstone	Red, purple sandstone
Ramim–Manara	IP24	Naftali Mountains, Upper Galilee	35.559901	33.201915	Hydra, Lower Cretaceous	Sandstone	Red, brown sandstone
Ahihud Forest	IP25	Western Galilee	35.174896	32.905947	Taqiyya, Paleocene to Early Eocene	Marl and chalk	Iron nodule
Ahihud Forest	IP26	Western Galilee	35.174896	32.905947	Taqiyya, Paleocene to Early Eocene	Marl and chalk	Iron nodule
Adulam	IP71	Judean foothills, Shephelah	35.154989	30.347713	Adulam, Early to Middle Eocene	Limestone and hard chalk	Brown, rusty, iron nodule
Adulam	IP72	Judean foothills, Shephelah	35.154989	30.347713	Adulam, Early to Middle Eocene	Limestone and hard chalk	Gray concentric, iron nodule
Arad	IP33	Judean Desert, Northern Negev	35.21911	31.24608	Shivta, Turonian	Dolomitized limestone	Brown, orange with conchoidal fracture
Arad	IP34	Judean Desert, Northern Negev	35.25761	31.01397	Shivta, Turonian	Dolomitized limestone	Brown, orange with conchoidal fracture
Nekarot	IP35	Negev Desert	35.078208	30.643914	Shivta, Turonian	Dolomitized limestone	Yellow friable
Nekarot	IP36	Negev Desert	35.078208	30.643914	Shivta, Turonian	Dolomitized limestone	Brown, yellow friable
Nekarot	IP37	Negev Desert	35.078208	30.643914	Shivta, Turonian	Dolomitized limestone	
Nekarot	IP38	Negev Desert	35.078211	30.644197	Shivta, Turonian	Dolomitized limestone	Brown, black dense
Nekarot	IP39	Negev Desert	35.081905	30.644635	Shivta, Turonian	Dolomitized limestone	Black dense
Nekarot	IP40	Negev Desert	35.083615	30.645441	Shivta, Turonian	Dolomitized limestone	Brown, black dense
Nekarot	IP61	Negev Desert	35.078211	30.644197	Shivta, Turonian	Dolomitized limestone	Black dense
Nekarot-Evus	IP41	Negev Desert	35.043867	30.57382	Shivta, Turonian	Dolomitized limestone	Brown, orange
Nekarot-Evus	IP42	Negev Desert	35.043867	30.57382	Shivta, Turonian	Dolomitized limestone	Brown associated with
Nekarot-Evus	IP43	Negev Desert	35.041301	30.573553	Shivta, Turonian	Dolomitized limestone	Black dense
Nekarot-Evus	IP44	Negev Desert	35.041301	30.573553	Shivta, Turonian	Dolomitized limestone	Black dense
Dimona–Sdom Rd	IP45	Negev Desert	35.015272	31.000492	Tamar, upper Cenomanian	Dolomitized limestone	Red sandstone
Eshet	IP46	Negev Desert	35.154988	30.347713	Tamar, upper Cenomanian	Dolomitized limestone	Yellow rusty
Eshet	IP47	Negev Desert	35.154988	30.347713	Tamar, upper Cenomanian	Dolomitized limestone	Brown rusty
Eshet-Ora Fm.	IP48	Negev Desert	35.147016	30.342962	Ora, lower Turonian	Marls	Brown rusty

(Continued)

TABLE 1 (Continued)

Ore body	Sample No.	Geographic region	GPS coordinates		Geological formation/ age	Hosting rock	Description
Zvar Habaqbuq/Paran	IP21	Negev Desert	35.024059	30.317927	Tamar and Ora, Cenomanian and lower Turonian	Dolomite, Marls, Dolomitized limestone	Black, brown dense
Zvar Habaqbuq/Paran	IP22	Negev Desert	35.024059	30.317927	Tamar and Ora, Cenomanian and lower Turonian	Dolomite, Marls, Dolomitized limestone	Brown dense with a conchoidal fracture
Zvar Habaqbuq/Paran	IP49	Negev Desert	35.024059	30.317927	Tamar and Ora, Cenomanian and lower Turonian	Dolomite, Marls, Dolomitized limestone	Black, brown dense with conchoidal fracture
Mishchor	IP50	Ramon Crater	34.89118	30.61969	Jurassic-Triassic boundary	Laterite	
Timna	IP51	Arabah Valley	34.946432	29.795806	Amir-Avrona	Sandstone	Iron nodule
Timna	IP52	Arabah Valley	34.948919	29.800381	Amir-Avrona	Sandstone	Iron nodule
Timna	IP63	Arabah Valley	34.948919	29.800381	Amir-Avrona	Sandstone	Iron nodule
Wadi Amram	IP62	Arabah Valley	/	/	Amir-Avrona?	Sandstone?	Iron nodule
Ajlun	IP27	Ajlun, Jordan	/	/	Limestone formation -Cenomanian, Turanian	Limestone	Black, brown
Ajlun	IP28	Ajlun, Jordan	/	/	Limestone formation -Cenomanian, Turanian	Limestone	Black dense
Ajlun	IP64	Ajlun, Jordan	35.713276	32.223214	Limestone formation -Cenomanian, Turanian	Limestone	Reddish, brown rusty
Ajlun	IP65A	Ajlun, Jordan	35.713312	32.223214	Limestone formation -Cenomanian, Turanian	Limestone	Black dense with white calcite veins
Ajlun	IP65B	Ajlun, Jordan	35.713312	32.223214	Limestone formation -Cenomanian, Turanian	Limestone	Brown dense with a conchoidal fracture

the Turonian age and the Taqiyya Formation of Paleocene age, which are geographically widespread. Epigenetic hydrothermal deposits are associated with major trending faults such as the Dead Sea Transform in the Negev Desert in Israel and in the Ajlun region, Jordan.

A short description of the samples collected for this study follows.

2.1.1. Sedimentary deposits

Sedimentary deposits are aeolian iron concretions formed by the chemical interaction of paleo-groundwater with iron minerals in porous sedimentary rocks. The concretions record a history of iron mobilization and precipitation caused by changes in oxidation conditions, pH, and bacterial activity (Ilani et al., 2020).

2.1.2. Ramim–Manara ridge

The ore deposit is situated in the Naftali Mountains of Upper Galilee and stretches from the northern tip of modern Israel into Lebanon. It is an aeolian sedimentary source built up of two layers, with a maximum thickness of approximately 1.2 m extended over 4 km. These layers contain ferrous minerals (mainly goethite) dating to the Albian period (Lower Cretaceous). During the 1950s, trenches and tunnels were made in a prospecting study. An average iron content of 25–28 wt% was estimated, and an overall quantity

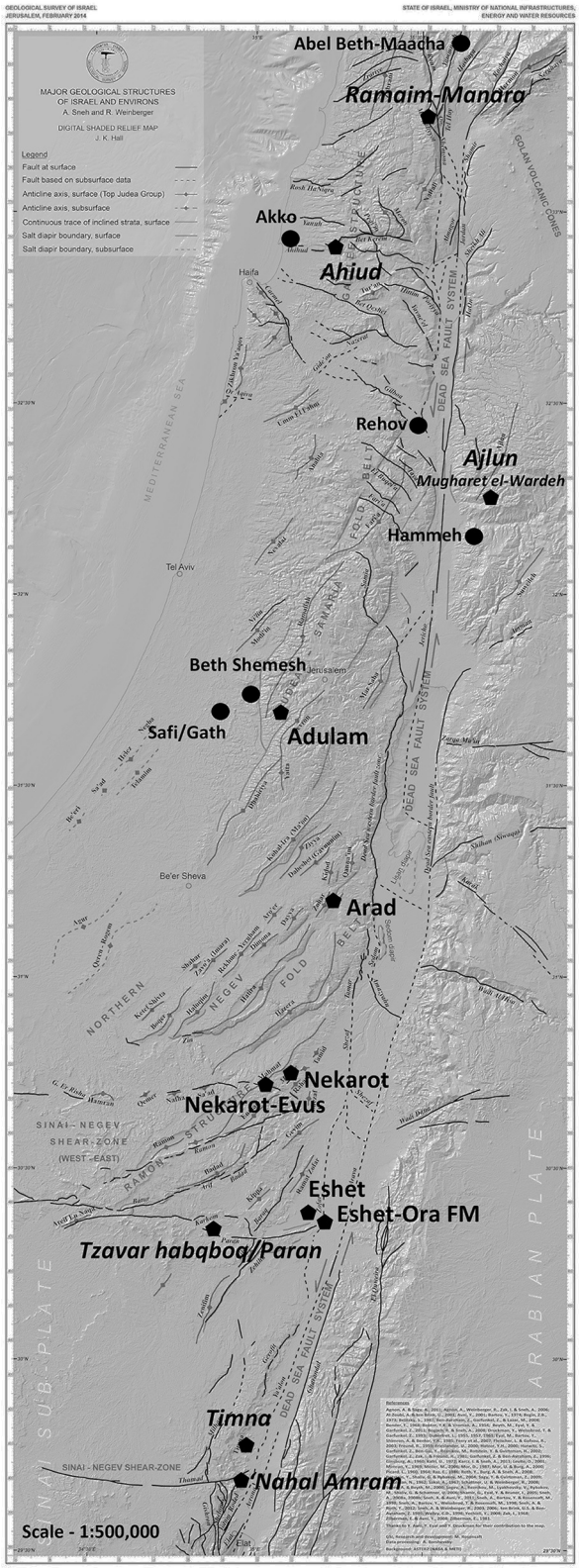

FIGURE 1
Map of Southern Levant, showing the location of the iron ores used in the study. Also marked are Iron Age sites, mentioned in the text.

of 40 tons. Due to its relatively low iron concentration and the need for sub-surface mining, it was never exploited (Ilani, 1989). Two samples were collected; Sample IP23 is a reddish-purple sandstone from an exposed vein parallel to the cliff, and Sample IP24 was carved from the rocks at the entrance to the prospect tunnel (Figure 2).

2.1.3. Ahihud

The sampling location was chosen where a section in the Taqiyya Formation was exposed during construction works in the area. The Taqiyya Formation, of the Paleocene to the early Eocene age, is a massive unit of white-gray friable soft marl and chalk, in which brown to yellow-ochre oolitic iron was concentrated as concentric nodules. The mineralogy was mainly characterized by fossilized goethite, with low quartz, calcite, and clay associated. The average iron content was estimated to be lower than 30 wt%; however, some highly concentrated nodules were noted. Similar oolitic iron is also known from other locations in Central Galilee, such as the two samples analyzed in this research (Samples IP25 and IP26, ~80 wt%; see the following discussion). The samples for this study were carved out easily from the soft chalk (approximately 0.5 kg in 15 min of work by a single individual) and assigned as Samples IP25 and IP26.

2.1.4. Adulam Formation (Elah Valley)

The Adulam Formation of the early to middle Eocene age overlies the Taqiyya Formation and is widely exposed in the western Judean foothills. It is characterized by bedded limestone and hard chalk, containing lenses of chert and occasionally also oolitic/concretions of iron similar to the previously mentioned deposits in the Taqiyya Formation, and is often associated with the mineral barite ($BaSO_4$). Samples IP71 and IP72 were collected at the western–northern part of the Elah stream, where the formation is widely exposed, close to the Iron Age IIA sites of Khirbet Qeiyafa and Tel Beth-Shemesh (Figure 1).

2.1.5. Arabah Ores—Timna and Wadi 'Amram

Four samples of ferruginous iron-rich nodules were collected from the Arabah valley. These were formed through epigenetic remobilization, weathering, and erosion of the primary copper–iron (Cu-Fe) sulfidic ores of the Amir/Avrona Formation (Hauptmann, 2007, p. 63–68). Three samples were collected below the archaeological copper mining fields of Merkavot (IP51–52 and IP63). Sample IP62 was collected at Wadi 'Amram, also a historical copper mining site. Mineralogically, they are dominated by quartz sand, contain an average of 20 to 30 wt% iron and minor anhydrite and calcite, and often have relatively high copper concentrations (between 1 and 4 wt% CuO; Ilani et al., 1985).

Additional sedimentary deposits were identified at Arad, Mishchor, the Dimona–Sdom Road, and the Ora Formation. These are minor deposits with low/very low iron content and therefore are not thoroughly discussed in this study.

2.1.6. Epigenetic hydrothermal deposits

Iron mineralizations of this type are restricted to regional tectonic lineaments. In the northern Sinai and the Negev Desert, they occur in carbonate rocks of the Cretaceous Judea Group and were emplaced via a two-stage process involving an initial

10.3389/fearc.2023.1221130

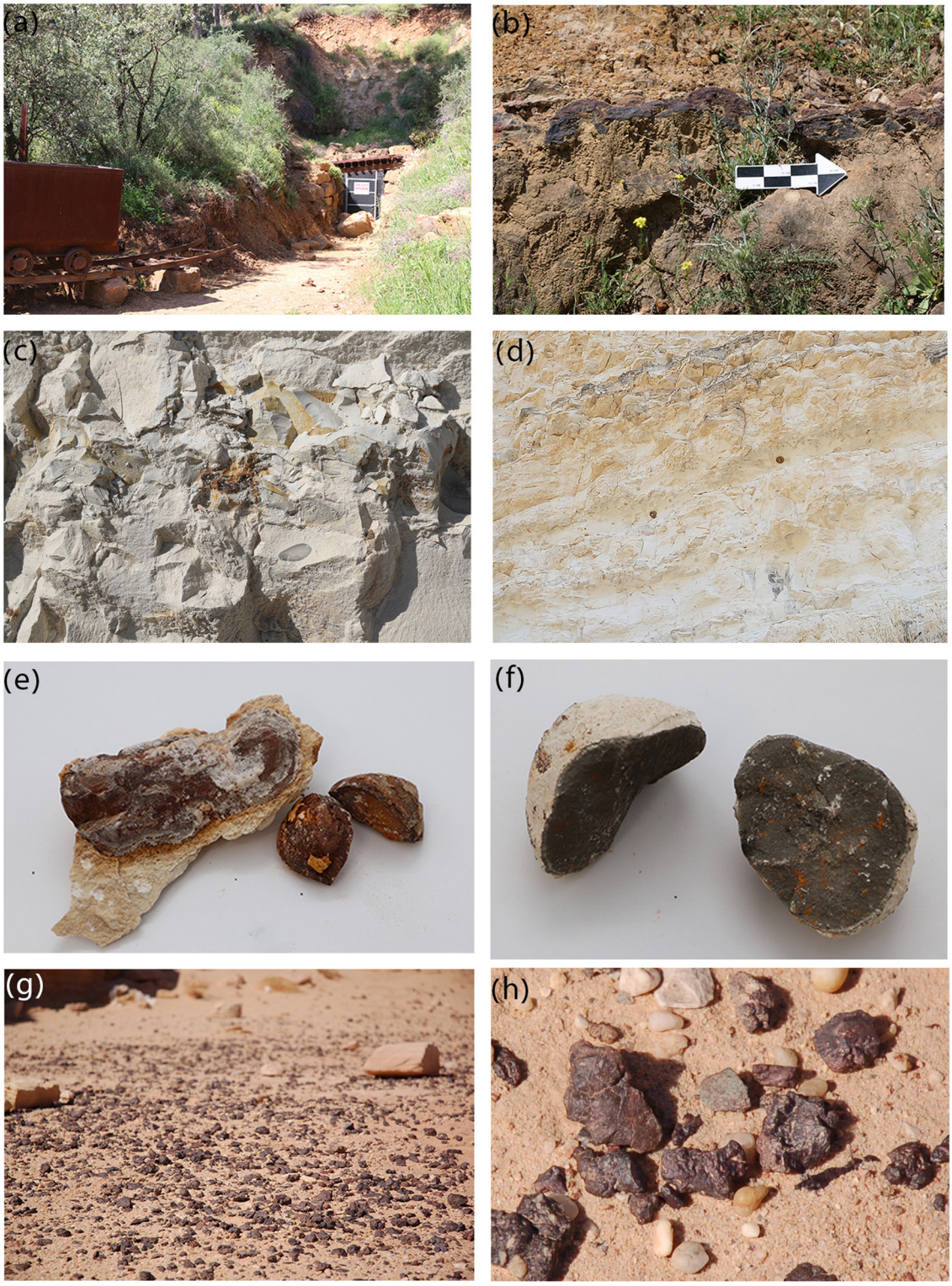

FIGURE 2
Field views of the major sedimentary ores analyzed in this study. **(a, b)** Manara–Ramim. **(c)** View of the Taqiyya Formation exposure at Ahihud forest; note the iron concretion at the middle of the white chalk. **(d)** View of the Adulam Formation; note the two small iron concentrations seen as brown dots. **(e)** Sample IP72. **(f)** Sample IP71 (pyrite) collected from Adulam Formation; **(g, h)** iron nodules scattered at the surface, Timna.

step of dolomitization followed by the mineralization of the iron vein and trace metal enrichment. The Negev Desert consists of a series of east–west shear faults located between the head of the Aqaba Gulf and the northern Arava Valley, dissected by the north–south Dead Sea Transform segments of the African–Arabian plate boundary (Erel et al., 2006; Grosz et al., 2006; Ryb, 2008; Ryb

et al., 2022). Hydrothermal solutions containing high percentages of iron moving upward through these faults had partially replaced the limestone in the massive carbonate rock and precipitated to form the iron-ore body. Several mechanisms were suggested for the formation of these ores, and studies of their paragenesis show variability in the associated minerals and especially in their iron content (Ilani et al., 1985; Ilani, 1989; Erel et al., 2006; Ryb, 2008).

2.2. Negev deposits

2.2.1. Wadi Nekarot and Nekarot-Evus

The iron deposits of these two locations are associated with the Shivta Formation and the Tamar Formation. In the Nekarot stream, iron-bearing lenses, which are up to 2 m wide and 80 m long, appear along the Ramon fault (Samples IP35-IP40 and IP61). At the junction of the two streams, Nekarot and Evus, fragmented ore chunks are widely dispersed on the surface of a small hill (Figure 3). These samples (IP41–IP44) are characterized by a striking black color and are substantially enriched with iron.

2.2.2. Zvar Habaqbuq/Paran

This deposit is located along the eastern part of one of the major faults in the Negev desert, the Paran fault, and is situated at the base of the Menuha Ridge segment. The Paran deposit was prospected in the early 1950s, and two shafts were carved down to its base, as well as a section trench. Despite being the most significant deposit in Israel, it was never economically exploited. The deposit appears between the Tamar Formation and the Ora Formation and comprises three main minerals, namely, hematite, goethite, and hematitic jasperoids (Ilani 2004). Three samples (IP21–22 and IP49) were analyzed from this deposit.

2.2.3. Eshet Dome–Ora formation

This deposit is situated approximately 10 km to the east of the Zvar Habaqbuq deposit along the Paran fault. Eshet Dome was also previously prospected (Figure 3). Two samples (IP46 and IP47) were analyzed from this location. On the trail pass to Eshet Dome, iron-rich nodules associated with the Ora Formation were also sampled (IP48).

2.2.4. The Ajlun deposit: Mugharet el-Wardeh (Jordan)

The iron-ore body of Mugharet el-Wardeh is a massive lenticular body approximately 300 m by 200 m, with a maximum thickness of up to 10 m, and is exposed and accessible at the surface in a few locations (Figure 3). It is predominantly composed of hematite, with lesser amounts of goethite and limonite, as well as calcite, quartz, and chalcedony in minor amounts (Bender, 1968). As these were formed by the upward movement of iron-rich hydrothermal solutions that replaced the hosting carbonate rocks, it is occasionally enriched with calcite. Al-Amri (2008) reports an average ($n = 24$) iron oxide (Fe_2O_3) content of 81.5 wt%, which he claims is the highest iron oxide value ever reported from ore mineralizations in the area of the Southern Levant. Five samples (IP27–28, IP64, and IP65A–B) were analyzed from this deposit.

2.3. Hematite artifacts

Hematite and other iron minerals (as well as simply dark stones) were used in different periods for various purposes, such as mace heads, scale weights, and hammerstones. The stones were rarely analyzed (but see Al-Amri, 2008), and the sources of the minerals are mostly unknown. For this study, we selected hematite artifacts from three Iron Age sites. The artifacts, originating from Tel Abel Beth Maacah, Tel Rehov, and Tell es-Safi/Gath, are listed with the registration data in Table 2, and some are shown in Figure 4.

3. Analytical methods and data analysis

Freshly broken fragments from the interior of the selected specimens were finely ground in an agate mortar to obtain a fine powder, which was then divided for the various analyses. We used XRD and FTIR to identify the major mineralogical components of the ores. XRD analyses were carried out using a Rigaku SmartLab SE instrument, with copper K-α radiation at 40 kV/50 mA. Powdered samples (prepared as pellets) were measured in a 2Theta/Theta mode between 10/15 and 75 degrees at a scan speed of 5/min and a scan step of 0.02.

FTIR spectra were obtained by grinding the samples with KBr (IR-grade) to produce a 5-mm-diameter pellet using a hand press. Representative spectra were collected between 4,000 and 400 cm^{-1} at 4 cm^{-1} resolution for 32 scans using a Thermo iS5 spectrometer (Thermo Fisher Scientific, Waltham, MA, USA). The interpretation of spectra is based on a library of mineral standards. The advantage of this method lies in the quick, easy gathering of information and its sensitivity to disordered phases, thus making it complementary to XRD. A summary of the results is given in Table 3.

To directly measure the chemical composition including that of silica and carbonates, samples were subjected to LA-ICP-MS. Analyses were performed at the Curt-Engelhorn-Center of Archaeometry, Mannheim, Germany, along with the Os isotope analysis. The analysis was conducted using an iCAP Q ICP-MS (Thermo Fisher Scientific) and a 193-nm ArF laser ablation system (ATLSI300, RESOlution M-50).

Os isotopic composition ($^{187}Os/^{188}Os$) and Os concentrations were measured following a standard procedure (Brauns et al., 2000; Brauns, 2001). For analyses, powdered iron-ore samples (300 mg) were weighed into pre-spiked ($^{185}Re/^{190}Os$ tracer with $^{185}Re/^{190}Os = 10.3$) Carius tubes, followed by dissolution and equilibration with inverse aqua regia at 240 °C. Os was extracted by distillation of the volatile tetraoxide, condensed on a small volume (10 µl) of chilled H_2SO_4, and then collected in 2 mL of 6.8 N HBr. Final purification of Os was done by micro distillation (Birck et al., 1997). Os isotope ratios were measured by ion counting on a modified Finnigan-MAT 261 operated in jump mode, corrected for mass bias and oxides. Internal (2 *SD*) precision for unknowns was < ±0.3%. Final $^{187}Os/^{188}Os$ ratios are corrected for blank (0.075 ±

10.3389/fearc.2023.1221130

FIGURE 3
Field views of the major Hydrothermal ores analyzed in this study. **(a, b)** the exposed surface vein of Nekarot. **(c, d)** The geological fault at Nekarot-Evus and the ore scattered at the top of the hill. **(e, f)** The shaft created in the 1950s at the Zvar Habaqbuq/Paran deposit and a close-up view of the section. **(g, h)** View at the piles of ores and a close-up from the former Mugharet el-Wardeh cave, Ajlun, Jordan.

0.05 pg Os, $^{187}Os/^{188}Os$ blank: 0.108) assuming an Os yield of 85% (Brauns, 2001). Blank contribution to the samples in this work was negligible, below 0.5%.

Trace and rare earth elements (REEs) composition analyses were conducted on 7500 cx Agilent ICP-MS at Hebrew University. Approximately 1 g of fine powder was weighed, mixed with

TABLE 2 List of hematite objects and their registration information.

Site name	Sample no.	Locus no.	Basket no.	Stratum	Period	Publication
Abel Beth Maacah	HEM1	5759	57348		Iron IIA	Unpublished
Tel Rehov	HEM2	5034	50214	VI	Iron IIA	Kletter, 2020: Cat 16
Tel Rehov	HEM3	9434	94312	IV	Iron IIA	Kletter, 2020: Cat 17
Tel Rehov	HEM4	7050	70305/2	IV	Iron IIA	Kletter, 2020: Cat 18
Tel Rehov	HEM5	7050	70305/1	IV	Iron IIA	Kletter, 2020: Cat 22
Tel Rehov	HEM6	7050	70305/3	IV	Iron IIA	Kletter, 2020: Cat 23
Tel Rehov	HEM7	6411	64799	IV	Iron IIA	Kletter, 2020: Cat 28
Tel Rehov	HEM8	6411	64807	IV	Iron IIA	Kletter, 2020: Cat 29
Tell e-Safi/Gath	HEM9	D15BD02	D15BD005	D-3	Iron IIA	Unpublished; Courtesy of Aren Maeir, Bar Ilan University
Tell e-Safi/Gath	HEM10	149709	1497046	D-3	Iron IIA	Unpublished; Courtesy of Aren Maeir, Bar Ilan University
Tell e-Safi/Gath	HEM11	119603	1196029	D-3	Iron IIA	Unpublished; Courtesy of Aren Maeir, Bar Ilan University
Tell e-Safi/Gath	HEM12	D15BD02	D15BD006	D-3	Iron IIA	Unpublished; Courtesy of Aren Maeir, Bar Ilan University
Tell e-Safi/Gath	HEM13	19D93B02	19D93B016	D-3-4	Iron IIA	Unpublished; Courtesy of Aren Maeir, Bar Ilan University

FIGURE 4
Hematite objects from Tel Rehov, HEM3, HEM4, and HEM6.

0.5 M acetic acid in excess, and placed in a hot bath for 24 h in order to dissolve the carbonates. When completed, samples were washed using double-distilled water (<18 MΩ cm^{-1}), dried, and weighed again. Approximately 100 mg of the carbonate-free sample was treated with 5 mL concentrated (9.5 N) HCl (in a hot bath for 8 h) to dissolve the oxides. When cooled, 0.5 mL of the supernatant was further diluted to a final volume of 10 mL, of which 2–3 mL was used for the analysis. Prior to the analysis, the ICP-MS was calibrated with a series of multielement standard solutions for trace and rare elements and REEs (Merck; ME VI). A solution of internal standards (750 µg/L Sc, 100 µg/L Re, and 50 µg/L Rh) was injected alongside the samples during the analytical session for drift and matrix correction. The contribution of metals by the reagents used in the procedures was determined by measuring procedural blanks. For precision and detection-limit estimation, the blank and two selected standards were remeasured prior to approximately every 20 samples and at the end of the analysis. In addition, for accuracy estimation, standard reference samples (U.S. Geological Survey standard reference sample T-235) were examined following calibration and at the end of the analysis.

In an attempt to further differentiate between the various ore deposits and find possible correlations between the ores and the hematite objects, the trace elements and REE data were examined using statistical methods.

The europium and cerium anomalies were calculated (Supplementary Table 1) using chondrite values (Piper and Bau, 2013). The concentration data were then rescaled using a centered-log ratio transformation and normalized using Z-score normalization (Aitchison, 1982). The transformed and scaled data were then used for calculating the pairwise Euclidean distance (PED) between each pair of samples, as well as the mean values for each group. In this representation, similar samples have small pairwise distances and hence appear in the matrix as blue pixels, whereas samples that are different from each other are characterized by high values of pairwise distance and are hence represented as orange and yellow pixels.

Following the calculation of the distance matrix and the average distance between groups, we used hierarchical clustering to present the data as a dendrogram. This approach is applicable for provenance studies because similar samples cluster close to each other and appear on branches that are separated by short lines, whereas specimens that are less similar appear on branches separated by long lines that split close to the beginning of the tree (e.g., Finkel et al., 2022). The cophenetic correlation metric is used to evaluate the reliability of the dendrogram and its ability to represent the multidimensional structure of the data using a two-dimensional figure. The same procedure was repeated with the hematite objects' data in order to determine which ore samples are most similar to the excavated artifacts.

The relative importance of key siderophile (cobalt, nickel, and molybdenum), lithophile (vanadium, chromium, manganese, and barium), and chalcophile (copper) elements in distinguishing ores was considered by examining the differences between the ores (at

TABLE 3 Major mineralogical phases determined by X-ray diffraction (XRD) and Fourier-transform infrared (FTIR) spectroscopy (some from Stepanov et al., 2020).

Ore body	Sample no.	Main mineralogical phases by FTIR, XRD							
		Hm	Gth	Cal	Gy/An	Qtz	Brt	Cly	Pyr
Ramim–Manara	IP23–24	x	x	xxx		xxx			
Ahihud Forest	IP25–26		xxx						
Adulam	IP71–72		xxx				x		xx
Arad	IP33–34	tr	x	xx		tr			
Nekarot	IP35–40, 61	x	xxx	tr		xx	x/tr		
Nekarot-Evus	IP41–44		xxx	x	tr	x	tr		
Dimona-Sdom Rd	IP45		tr			xxx			
Eshet	IP46–47	xx	xx	tr	xx				
Eshet Dome–Ora Formation	IP48	tr	xxx						
Zvar Habaqbuq/Paran	IP21, 49	xx	xxx		tr	x			
Zvar Habaqbuq/Paran	IP22	x	x			xxx			
Mishchor	IP50	x						xxx	
Timna	IP51–52, 63	x	x		tr	xxx	tr		
Wadi Amram	IP62	x	x	tr		xxx			
Ajlun	IP27–28, 64–65	xxx	xx	x		x			

x, xx, and xxx indicate relative degree of mineral abundance in the sample. tr, only localized occurrence of mineral phase; Hm, hematite; Gth, goethite; Cal, calcite; Gy/Anh, gypsum/anhydrite, Qtz, quartz; Brt, barite; Cly, clay; Pyr, pyrite.

$\alpha = 0.05$) using the Kruskal–Wallis (KW; Kruskal and Wallis, 1952) test. The KW test provides a non-parametric alternative analysis of variance (ANOVA) and was followed by a *post-hoc* pairwise test conducted using the Dunn-Šidák correction for multiple comparisons (Šidák, 1967). The resulting multiple comparison plots portray the mean ranks of the data (after Centered log-ratio (CLR) transformation) and their confidence intervals, where groups that are significantly different (at $\alpha = 0.05$) can be distinguished.

4. Results

4.1. Ores

4.1.1. Mineralogy and major elements composition

Table 3 summarizes the major mineral components of the various ore deposits analyzed in this study. These are based on mineralogical characterization obtained by XRD and FTIR (some of which were previously published by Stepanov et al., 2020). Generally, the following minerals were identified: goethite and hematite as the major iron oxide phases and calcite, quartz, and occasionally barite and pyrite as secondary minerals. Some ores showed higher variability between samples, especially regarding the associated minerals and iron content. The chemical composition of the major elements as obtained by LA-ICP-MS, are presented in Table 4.

Among the sedimentary formations (Ramim–Manara, Ahihud, Adulam, Mishchor, Dimona–Sdom Road, Arad, and Timna), samples are generally iron-poor and more silica/carbonate-rich. This excludes the concentrated nodules of Ahihud and Adulam, where iron content was measured up to 70–80 wt% Fe_2O_3, and samples from Timna with an average iron oxide content of approximately 60 wt%. The two Ahihud samples (IP25 and IP26) are very similar and are clearly dominated by goethite, with hardly any associated minerals. The two samples from Adulam differed from one another; one was identified as goethite (IP72), and the other was almost pure pyrite (IP71). The Ramim–Manara Ridge samples (IP23 and IP24) are composed of brown-reddish to purple sandstone; they are silica-rich (~30–40 wt%), and indeed, both FTIR and XRD show a high abundance of quartz.

The ferruginous nodules from the Arabah Valley (Timna and Wadi Amram) reveal an average of ~65 wt.% iron oxide (Fe_2O_3) as goethite and hematite, with significant levels of silica, an average of ~25 wt.% as quartz sand, and low levels of calcium oxide (CaO) (approximately 2 wt.%), correlating with the lack of carbonate minerals (Table 4). Note the high concentration of copper in the Arabah, approximately 2 wt% in Timna and 0.14%.wt in Wadi Amram. Furthermore, increased concentrations (in ppm) levels of lead, zinc, nickel, silver, and antimony were identified.

The Negev samples are on average highly rich in iron (approximately 80 wt.%). Elevated levels of barium were identified, especially in Nakarot and Nekarot-Evus ores, which is in agreement with the presence of barite as an associated mineral (Table 4). Their mineralogy includes goethite as the main ore mineral that

TABLE 4 Major elements composition of the studied ores analyzed by laser ablation inductively coupled plasma mass spectrometry, given in wt%.

Ore body	Sample No.	Na_2O	MgO	Al_2O_3	SiO_2	P_2O_5	K_2O	CaO	TiO_2	MnO	Fe_2O_3	BaO	CuO	ZnO	Total
Ramim/Manara	IP23	0.06	0.05	5.57	**39.92**	0.17	0.24	**0.51**	1.30	0.01	**52.09**	0.01	0.00	0.00	99.91
Ramim/Manara	IP24	0.01	0.50	3.22	**33.18**	0.12	0.12	**32.23**	0.41	0.09	**29.80**	0.01	0.00	0.06	99.75
Ahihud forest	IP25	0.03	0.43	0.76	**15.80**	0.25	0.08	**0.77**	0.04	0.01	**80.65**	0.75	0.05	0.14	99.75
Ahihud forest	IP26	0.03	0.44	0.57	**12.85**	0.16	0.06	**0.65**	0.03	0.00	**84.16**	0.70	0.04	0.12	99.82
Ahihud forest (average, $n = 2$)		0.03	0.43	0.67	**14.33**	0.20	0.07	**0.71**	0.03	0.01	**82.41**	**0.73**	0.05	0.13	99.78
Adulam	IP72	0.13	0.55	0.38	**14.92**	0.13	0.08	**2.33**	0.01	0.00	**67.95**	13.95	0.14	0.23	100.81
Arad	IP33	0.04	0.79	0.83	**8.83**	0.31	0.09	**54.71**	0.03	0.02	**33.79**	0.05	0.01	0.04	99.54
Arad	IP34	0.10	1.13	1.29	**7.91**	6.07	0.08	**19.94**	0.14	0.04	**58.48**	3.54	0.01	0.20	98.93
Arad (average, $n = 2$)		0.07	0.96	1.06	**8.37**	3.19	0.09	**37.33**	0.09	0.03	**46.14**	1.79	0.01	0.12	99.23
Nekarot	IP35	1.35	1.66	6.57	**14.61**	0.28	0.86	**0.86**	0.15	0.45	**68.76**	3.87	0.04	0.19	99.64
Nekarot	IP36	2.54	2.80	8.69	**24.71**	0.28	1.29	**3.98**	0.27	0.32	**53.87**	0.08	0.05	0.10	98.99
Nekarot	IP37	0.07	0.98	0.86	**6.59**	0.21	0.07	**1.58**	0.04	0.04	**88.84**	0.02	0.03	0.04	99.37
Nekarot	IP38	0.08	0.84	0.68	**5.75**	0.21	0.06	**4.24**	0.03	0.06	**87.24**	0.20	0.01	0.03	99.42
Nekarot	IP39	0.05	0.49	0.78	**8.82**	0.32	0.07	**1.71**	0.03	0.08	**78.12**	**9.36**	0.01	0.06	99.91
Nekarot	IP40	0.18	0.42	0.90	**3.11**	0.18	0.03	**0.73**	0.05	0.02	**93.98**	0.00	0.00	0.02	99.64
Nekarot (average, $n = 6$)		0.71	1.20	3.08	**10.60**	0.25	0.40	**2.19**	0.10	0.16	**78.47**	**2.25**	0.02	0.07	99.49
Nekarot-Evus	IP41	0.02	0.32	0.46	**20.69**	0.19	0.01	**2.89**	0.02	0.08	**73.69**	1.42	0.01	0.07	99.86
Nekarot-Evus	IP42	0.24	0.65	1.24	**3.99**	0.17	0.02	**3.45**	0.02	0.10	**82.28**	7.56	0.01	0.18	99.91
Nekarot-Evus	IP43	0.03	0.40	0.57	**3.89**	0.12	0.03	**2.99**	0.02	0.07	**89.95**	1.82	0.01	0.03	99.93
Nekarot-Evus	IP44	0.03	0.49	0.85	**4.11**	0.17	0.05	**6.38**	0.03	0.05	**86.51**	1.12	0.01	0.06	99.85
Nekarot-Evus (average, $n = 4$)		0.08	0.46	0.78	**8.17**	0.16	0.03	**3.93**	0.02	0.08	**83.11**	**2.98**	0.01	0.08	99.89
Meishar	IP45	0.02	0.08	0.29	**90.67**	0.07	0.02	**2.70**	0.09	0.04	**5.95**	0.03	0.00	0.00	99.96
Eshet	IP46	1.13	0.98	0.89	**1.86**	0.05	0.04	**18.17**	0.01	1.14	**75.60**	0.04	0.00	0.00	99.90
Eshet	IP47	0.31	0.80	1.50	**6.31**	0.19	0.13	**10.04**	0.43	0.18	**78.24**	0.02	0.00	0.01	98.15
Eshet (average, $n = 2$)		0.72	0.89	1.19	**4.09**	0.12	0.08	**14.10**	0.22	0.66	**76.92**	0.03	0.00	0.01	99.03

(Continued)

10.3389/fearc.2023.1221130

TABLE 4 (Continued)

Ore body	Sample No.	Na_2O	MgO	Al_2O_3	SiO_2	P_2O_5	K_2O	CaO	TiO_2	MnO	Fe_2O_3	BaO	CuO	ZnO	Total
Eshet Dome–Ora Formation	IP48	0.05	1.08	0.92	**5.82**	0.16	0.14	**3.31**	0.03	0.05	**87.77**	0.02	0.00	0.08	99.43
Mishchor	IP50	0.25	0.34	31.14	**51.02**	0.14	0.56	**0.56**	1.31	0.01	**14.36**	0.01	0.01	0.00	99.70
Zvar Habaqbuq/Paran	IP21	0.03	0.25	0.30	**3.59**	0.01	0.02	**0.55**	0.05	0.06	**94.88**	0.00	0.00	0.23	99.97
Zvar Habaqbuq/Paran	IP22	0.02	0.05	0.21	**73.08**	bdl	0.02	**0.39**	0.01	0.02	**26.14**	0.01	0.01	0.05	100.00
Zvar Habaqbuq/Paran	IP49	0.41	0.57	0.90	**5.67**	0.05	0.06	**5.31**	0.06	0.29	**83.38**	**2.42**	0.00	0.13	99.24
Zvar Habaqbuq/Paran (average, *n* = 3)		0.15	0.29	0.47	**27.45**	0.03	0.03	**2.08**	0.04	0.12	**68.13**	**0.81**	0.00	0.14	99.74
Timna	IP51	0.02	0.20	0.57	**18.91**	0.06	0.02	**2.77**	0.04	0.02	**73.58**	0.05	0.92	0.29	97.44
Timna	IP52	0.05	0.26	2.25	**30.87**	0.16	0.08	**2.27**	0.07	0.01	**56.92**	0.04	4.00	0.16	97.14
Timna	IP63	0.07	0.16	0.74	**26.39**	0.06	0.05	**1.53**	0.09	0.01	**65.51**	0.05	0.94	0.66	96.28
Timna (average, *n* = 3)		0.05	0.21	1.19	**25.39**	0.09	0.05	**2.19**	0.07	0.01	**65.34**	0.05	**1.95**	**0.37**	96.96
Wadi Amram	IP62	0.09	0.13	2.09	**14.53**	0.20	0.11	**0.95**	0.09	0.00	**78.91**	**1.78**	0.14	0.87	99.88
Ajlun	IP27	0.04	0.17	0.42	**5.80**	0.06	0.02	**14.39**	0.02	0.02	**79.03**	0.00	0.00	0.01	99.98
Ajlun	IP28	0.03	0.20	1.30	**4.67**	0.54	0.04	**0.63**	0.14	0.03	**92.34**	0.01	0.00	0.01	99.94
Ajlun	IP64	0.30	0.76	0.39	**2.18**	0.44	0.01	**33.56**	0.16	0.02	**62.09**	0.01	0.00	0.01	99.93
Ajlun	IP65A	0.03	0.09	0.14	**1.34**	0.03	0.00	**9.16**	0.02	0.00	**89.14**	0.00	0.00	0.03	99.99
Ajlun	IP65B	0.03	0.05	0.13	**0.74**	0.04	0.06	**0.09**	0.00	0.00	**98.86**	0.00	0.00	0.00	99.99
Ajlun (average, *n* = 5)		0.09	0.25	0.48	**2.95**	0.22	0.03	**11.57**	0.07	0.01	**84.29**	0.01	0.00	0.01	99.97

Bold values denotes the three main constituents.

10.3389/fearc.2023.1221130

TABLE 5 Osmium isotopic composition of iron ores and hematite objects analyzed for this study.

Sample name	Sample No.	$^{187}Os/^{188}Os$	2s	ppt Os	2s
Iron ores					
Ramim–Manara	IP23	0.7618	0.0023	111	1
Ramim–Manara	IP24	1.0641	0.0032	13	1
Ahihud forest	IP25	0.6766	0.0020	993	9
Ahihud forest	IP26	0.6445	0.0019	1,323	12
Adulam	IP71	0.6616	0.0020	227	2
Adulam	IP72	0.6288	0.0019	531	5
Arad	IP33	1.5016	0.0045	6,113	61
Arad	IP34	1.5562	0.0047	8,249	82
Nekarot	IP35	1.6946	0.0051	3,799	38
Nekarot	IP36	1.5733	0.0047	7,189	72
Nekarot	IP37	1.5057	0.0045	8,162	82
Nekarot	IP38	1.5207	0.0046	7,740	77
Nekarot	IP39	1.0876	0.0033	18,791	188
Nekarot	IP40	1.3436	0.0041	3,005	30
Nekarot	IP61a	1.0357	0.0031	18,932	176
Nekarot (replica)	IP61a	1.0357	0.0031	14,407	134
Nekarot	IP61b	1.0255	0.0031	14,983	150
Nekarot**	IP61a	1.0296	0.0031	15,067	140
Nekarot**	IP61b	1.0640	0.0032	13,683	127
Nekarot** average	IP61	1.0468	0.0032	14,375	133
Nekarot average		1.2651	0.0039	11,138	108
Nekarot STD		0.2644	0.0008	5,672	54
Nekarot-Evus	IP41	1.0185	0.0031	10,300	103
Nekarot-Evus	IP42	0.9564	0.0029	14,634	146
Nekarot-Evus	IP43	1.0383	0.0031	4,429	44
Nekarot-Evus**	IP43	1.0173	0.0031	6,089	57
Nekarot-Evus** (replica)	IP43	1.0145	0.0031	6,667	62
Nekarot-Evus** (average)	IP43	1.0159	0.0031	6,378	59
Nekarot-Evus	IP44	1.1157	0.0034	5,123	51
Nekarot-Evus (average)		1.0268	0.0031	7,874	77
Nekarot-Evus (STD)		0.0516	0.0002	3,890	40
Meishar	IP45	1.3805	0.0042	126	1
Eshet	IP46	2.1330	0.0065	134	1
Eshet	IP47	3.0554	0.0093	675	7
Eshet Dome–Ora formation	IP48	0.3781	0.0011	10,577	106
Zvar Habaqbuq/Paran	IP21	1.0717	0.0032	179	9
Zvar Habaqbuq/Paran	IP22	1.0591	0.0032	138	7
Zvar Habaqbuq/Paran	IP49	1.0437	0.0032	183	2
Zvar Habaqbuq/Paran**	IP49	1.0497	0.0032	157	1
Zvar Habaqbuq/Paran (Average)		1.0560	0.0032	164	5

(Continued)

TABLE 5 (Continued)

Sample name	Sample No.	$^{187}Os/^{188}Os$	2s	ppt Os	2s
Zvar Habaqbuq/Paran (STD)		0.0122	0.0000	21	4
Mishor	IP50	0.6905	0.0021	587	6
Timna	IP51	2.0260	0.0061	568	6
Timna	IP52	1.8635	0.0056	4,664	47
Timna	IP63	1.9745	0.006	755	7
Timna (average)		1.9547	0.0059	1,995	20
Timna (STD)		0.0830	0.0003	2,313	23
Wadi Amram	IP62	1.2396	0.0040	1,374	14
Wadi Amram (replica)	IP62	1.2418	0.0040	1,307	13
Wadi Amram (average)		1.2407	0.004	1,341	14
Ajlun	IP27	2.0556	0.0062	142	1
Ajlun	IP28	2.1378	0.0064	252	3
Ajlun	IP64	1.6067	0.0049	134	1
Ajlun	IP65A	2.4945	0.0076	155	1
Ajlun	IP65B	2.1205	0.0064	277	3
Ajlun–average		2.0830	0.0063	192	2
Ajlun–STD		0.3168	0.0010	67	1
Hematite objects					
Abel Beth Maacah	HEM 1	0.5131	0.0016	8,360	78
Tel Rehov	HEM 2	0.6677	0.002	807	7
Tel Rehov	HEM 3	2.0758	0.0063	434	4
Tel Rehov	HEM 4	0.9232	0.0028	317	3
Tel Rehov	HEM 5	0.7775	0.0024	29	0.3
Tel Rehov	HEM 6	0.7195	0.0022	21	0
Tel Rehov	HEM 7	0.501	0.0015	4,557	42
Tel Rehov	HEM 8	1.1298	0.0034	124	1
Tell e-Safi/Gath	HEM 9	0.5707	0.0017	244	2
Tell e-Safi/Gath	HEM 10	0.5474	0.0017	785	7
Tell e-Safi/Gath	HEM 11	1.6404	0.005	15.8	0.1
Tell e-Safi/Gath	HEM 12	0.63	0.0019	920	9
Tell e-Safi/Gath	HEM 13	1.0045	0.003	1,444	13

**denotes roasted ores used in the smelting experiments (from Brauns et al., 2020).

is occasionally intergrown with hematite. Based on previous XRD, FTIR, and scanning electron microscopy (SEM) analyses, quartz and calcite are the main associated non-metallic minerals, often in the form of lenses or veins, and small amounts of gypsum ($CaSO_4$) and barite ($BaSO_4$) are also commonly present (Stepanov et al., 2020). IP35 and IP36 were collected from a weathered yellow-ochre ore and show relatively lower iron oxide content of approximately 60 wt%, whereas the other samples (IP37–40) have iron oxide (Fe_2O_3) content, which, on average, is higher than 85wt%.

In the three samples (IP21, IP22, and IP49) collected from Zvar Habaqbuq and Paran, the ore can be divided into two main mineralogical associations. Samples IP21 and IP49 are fine-grained, black to dark-gray ores of high density, dominated by a mixture of hematite and goethite, with an average of approximately 90 wt% Fe_2O_3, while sample IP22 is a brown, less dense ore, characterized by conchoidal fracture upon breaking and is dominated by much higher quartz content of approximately 70 wt% (see Table 4).

The two samples (IP46–47) from Eshet Dome show high Fe_2O_3 content of slightly <80 wt% with relatively high silica content of approximately 12 wt% on average.

Five samples (IP27–28, IP64, and IP65A–B) from the Ajlun were studied, showing high iron content of approximately 85 wt% Fe_2O_3, generally elevated CaO levels of approximately 12 wt% on average (up to 33 wt% in IP64), which supports a

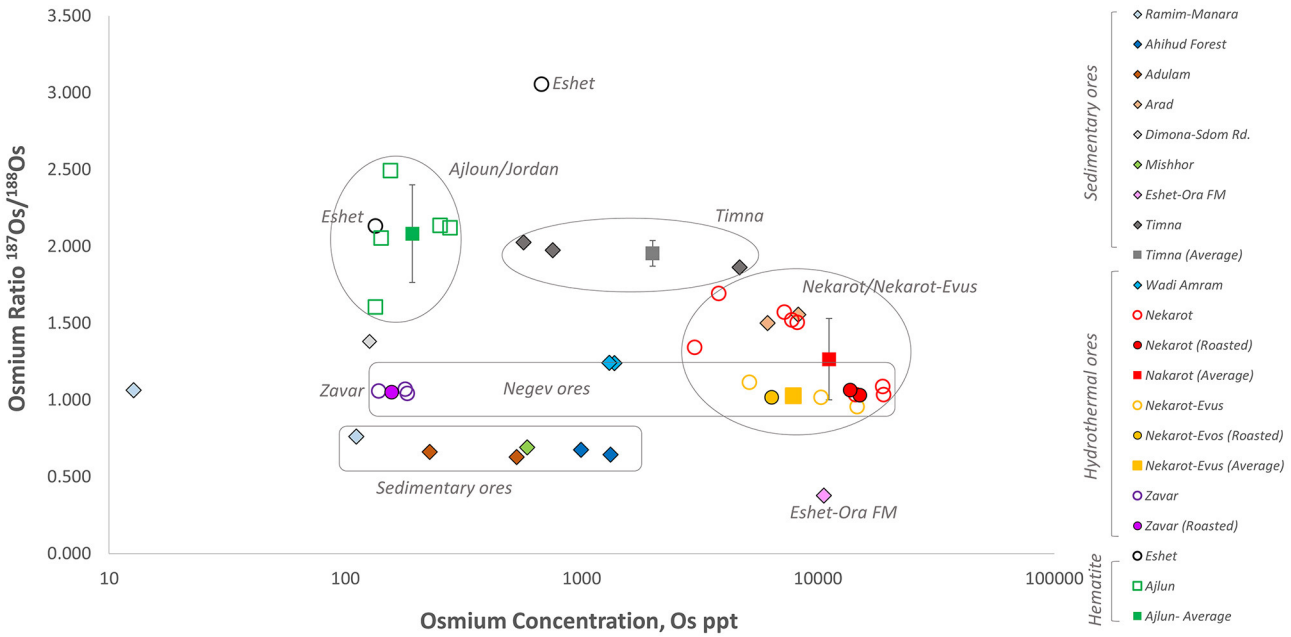

FIGURE 5
$^{187}Os/^{188}Os$ isotopic ratio of the iron ores analyzed in this study. Sedimentary ores are marked with diamond shapes. Hydrothermal ores in circles. Full circles denote ores roasted for the smelting experiments (from Brauns et al., 2020), and Ajlun samples are marked in a square. Also marked are averages and std deviations when applicable.

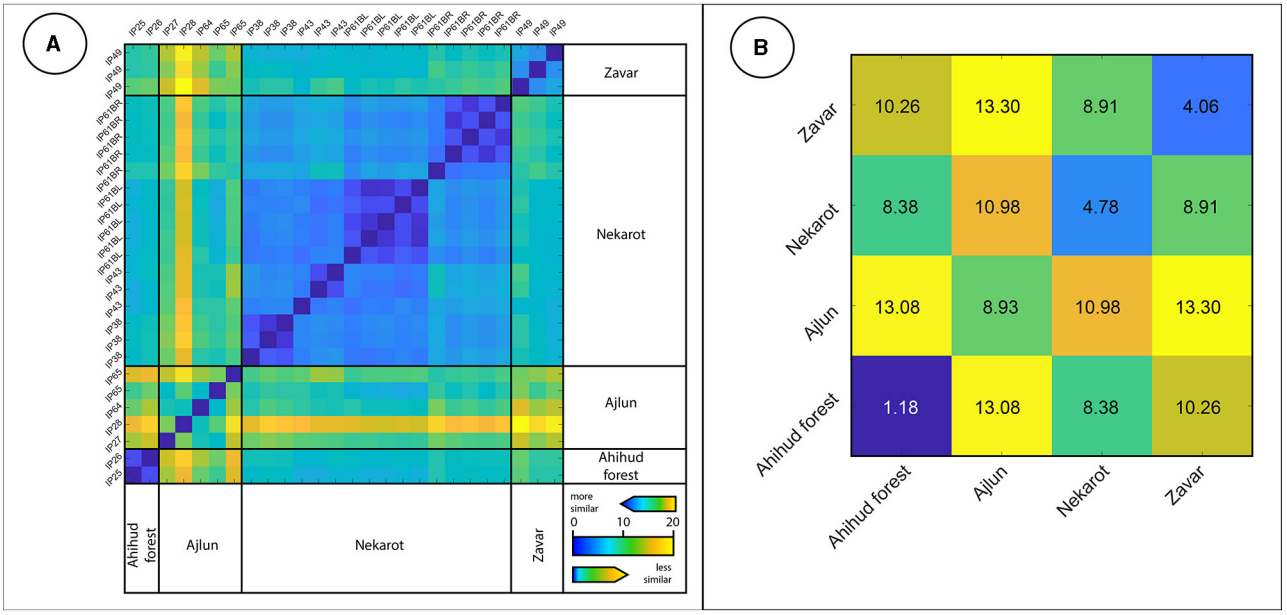

FIGURE 6
(A) The Euclidean pairwise distance matrix based on trace elements composition of the studied iron ores recovered from archaeological excavations. Similar specimens appear as blue pixels, whereas less similar specimens are depicted by yellow and orange pixels. **(B)** The mean Euclidean pairwise distance matrix of iron ores.

high amount of goethite and hematite minerals and calcite as the major associated minerals. The barium content of the Ajlun samples is clearly lower than those of the Negev ores, which correlates with the lack of gypsum and barite in the former (Table 4).

4.1.2. Os isotopic composition

A total of 43 ore samples were subjected to Os isotope analysis. The results are presented in Table 5. The Os isotopic ratios are shown against the Os concentrations in Figure 5. Using these two variables, a complex picture is obtained; however, some clusters

are formed, and several ore sources may be differentiated. The sedimentary ores of Ahihud, Adulam, Mishchor, and Eshet Dome–Ora Formation, as well as one sample from Manara–Ramim (IP23), have relatively low Os isotopic ratios ranging between 0.38 and 0.76, thus well separated from both the Negev and the Ajlun ores. Note the considerable variability in their Os concentration, which is correlated with their iron oxide content. Among the sedimentary ores, samples from Timna ($n = 3$) have generally high Os isotopic ratios, which overlap with the ratios measured in the Ajlun ores.

Although the Nekarot ($n = 10$) and Nekarot-Evus ($n = 5$) samples show some variability, they generally cluster together both in their isotopic ratios and Os concentrations. However, when large quantities were sampled (IP38/IP61 from Nekarot and IP43 from Nekarot-Evus, approximately 100 kg each) for the purpose of the smelting experiment and measured after roasting, these provided a much tighter cluster, approximately 1.05 $^{187}Os/^{178}Os$ (see IP43 and IP61; Brauns et al., 2020). Based on their similar mineralogy, chemical composition, and Os isotopic signature, the Nekarot and Nekarot-Evus ores are further treated as one group. While the three samples (IP21, IP22, and IP49) from the Zvar Habaqbuq/Paran deposit share similar Os isotopic values (with lower Os concentration) and are well separated from the Ajlun ores, the samples from Eshet do not. The latter have isotopic values, one that overlaps with the values of the Ajlun ores and one that is more radiogenic.

The Ajlun ores ($n = 5$) have higher average isotopic ratios (2.08 $\pm$ 0.3) than most of the sampled ores, with a partial overlap with the previously mentioned Nekarot, Eshet, and Timna ores.

Os concentrations can be used to differentiate between some of the overlapping ores. Such as in the case of Ajlun and Timna, Ajlun and Nekarot, and Nekarot and Paran. The two samples from Eshet are similar to the Ajlun ores in their Os concentration, rendering them inseparable from the Ajlun ores.

4.1.3. Trace element and REE composition of the ores

The EPD matrix, which was calculated based on trace elements concentrations and the europium and cerium anomalies (for the analytical results see Supplementary Table 1), demonstrates the relative homogeneity of each deposit (Figure 6). This is shown by the formation of blue rectangles along the diagonal (Figure 6A) and the increased mean distance of the groups compared with their own average (Figure 6B). The distribution of the specimens within the dendrogram (Figure 7) further points to their relative homogeneity, as well as a similarity between the groups, where the Nekarot ($n = 16$), Ahihud Forest ($n = 2$), and Zvar Habaqbuq ($n = 3$) specimens are all clustered, while the Ajlun samples ($n = 5$) are more spread out and isolated, indicating the heterogenic nature of the ore and its dissimilarity to the other studied sources.

The *post-hoc* analyses of the KW tests indicate that the differences between the groups are not significant at the $\alpha = 0.05$ level for vanadium, chromium, copper, and molybdenum, whereas cobalt, manganese, nickel, and barium show some significant differences between some of the groups (Figure 8).

4.2. Hematite artifacts

Figure 9 presents the EPD matrix and the mean distances between the hematite objects and the iron-ore deposits based on trace element composition. The yellow and orange pixels on the

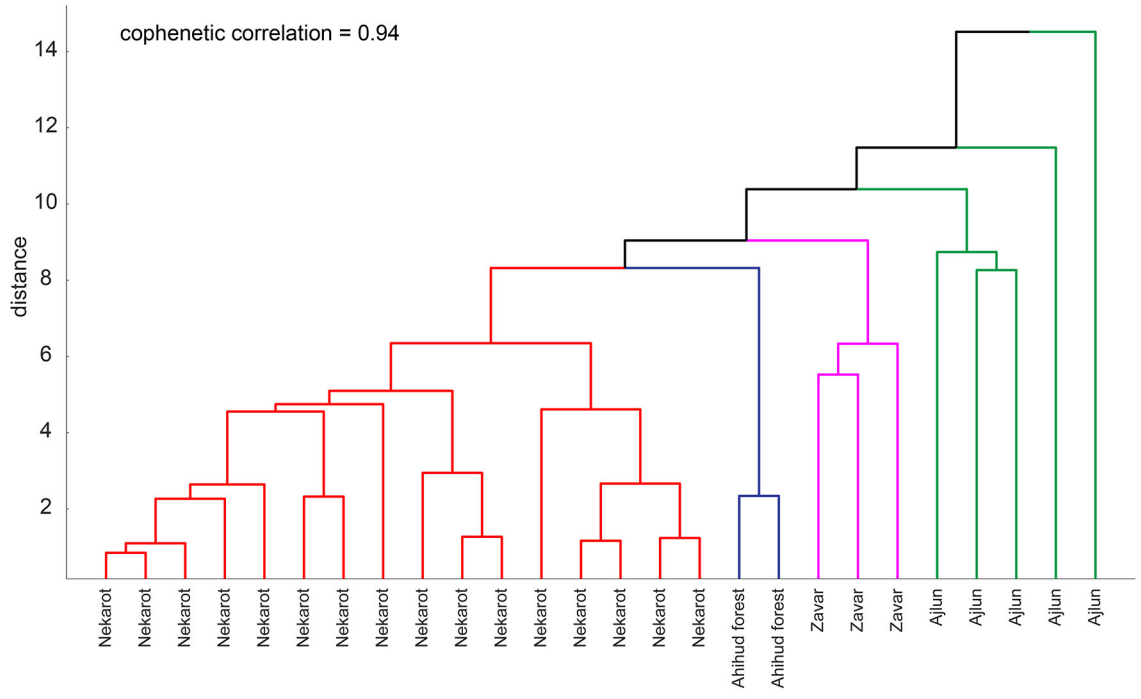

FIGURE 7
Dendrogram of the studied iron ores. Line colors depict the different studied source localities.

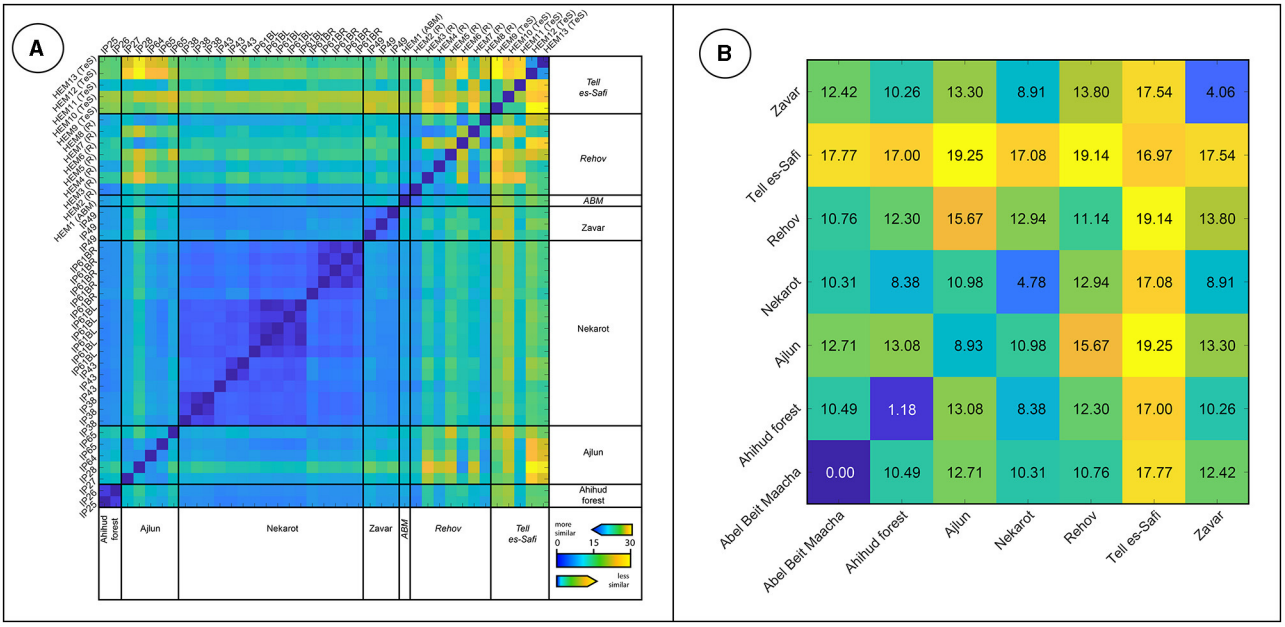

FIGURE 8
(A) The Euclidean pairwise distance matrix based on trace elements composition of the studied iron ores and hematite objects recovered from archaeological excavations. Similar specimens appear as blue pixels, whereas less similar specimens are depicted by yellow and orange pixels. **(B)** The mean Euclidean pairwise distance matrix of iron ores and hematite objects.

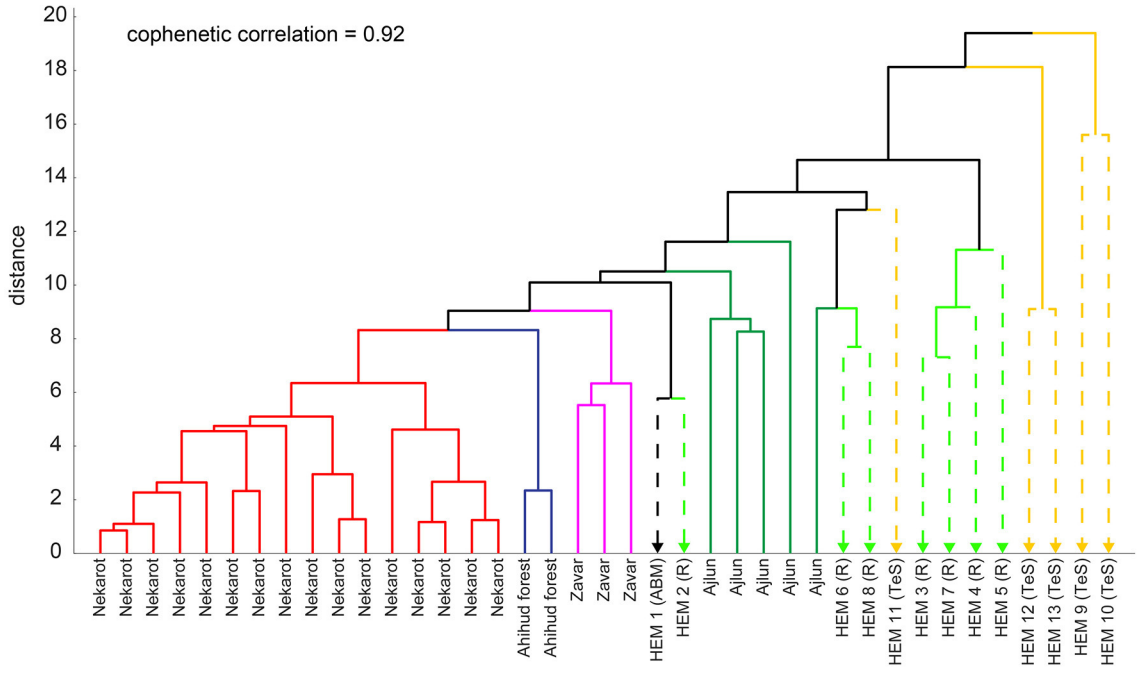

FIGURE 9
Dendrogram of the studied iron ores and hematite objects. Line colors depict the different studied source localities.

EPD matrix (Figure 9A) demonstrate the high heterogeneity of the hematite objects, with mean distances of the Tell es-Safi/Gath (17.0) and Rehov (11.1) objects (Figure 9B), which are substantially higher than those calculated for each of the studied iron-ore deposits (Figure 6). The studied groups of hematite objects are substantially different from each other, with mean distances ranging between 10.7 (between Rehov and Abel Beit Maacah) and 19.1 (between Tell es-Safi and Tel Rehov).

When plotted as a dendrogram, most of these artifacts do not cluster together with the studied ores and form a separate cluster

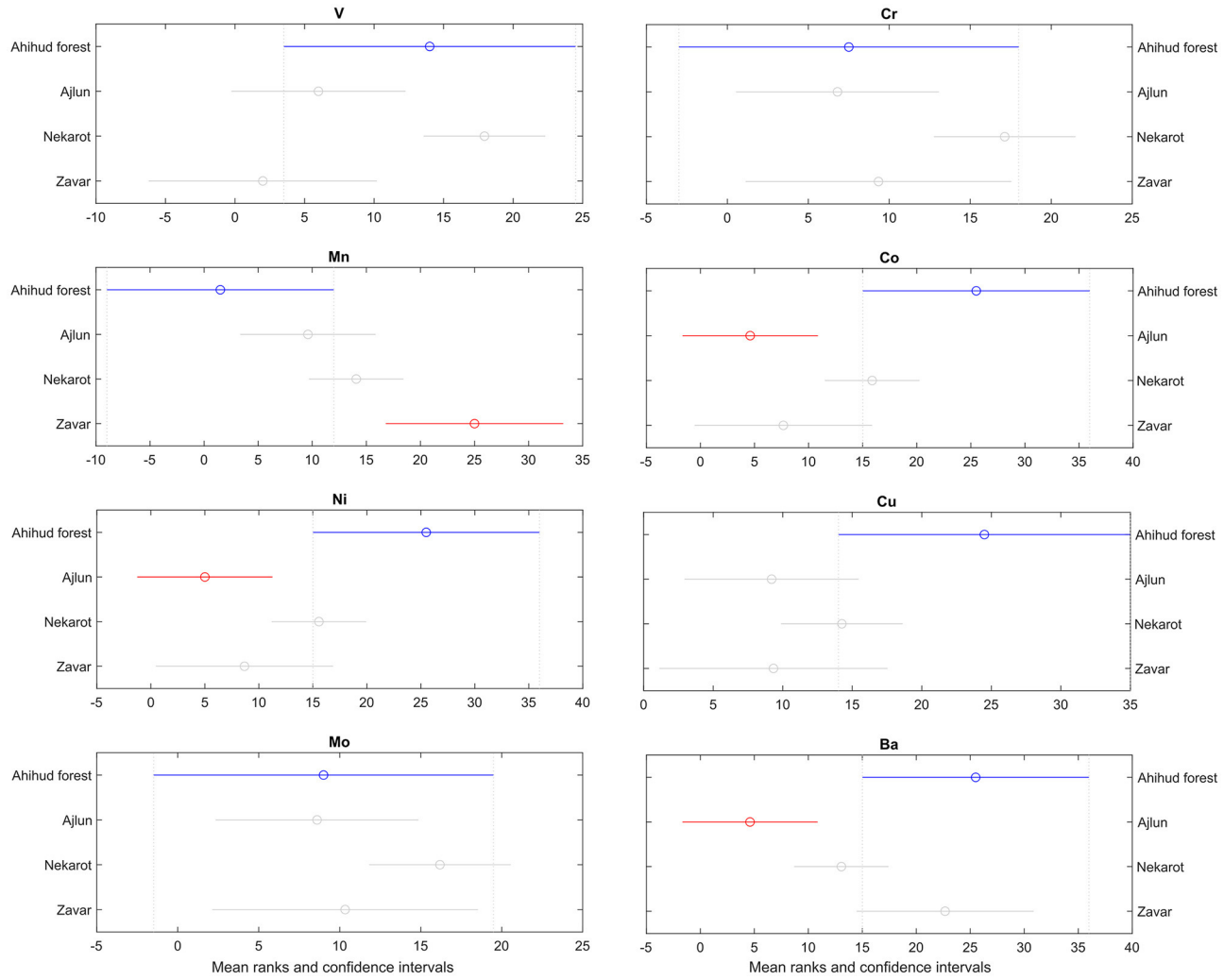

FIGURE 10
Multiple comparisons plots of key siderophile (cobalt, nickel, and molybdenum), lithophile (vanadium, chromium, manganese, and barium), and chalcophile (copper) elements, depicting the results of the Kruskal–Wallis (KW) test (Kruskal and Wallis, 1952) test and the *post-hoc* multiple comparisons test corrected utilizing the Dunn–Šidák approach (Šidák, 1967). The mean rank of the KW test and the confidence intervals for the ranks are depicted by a circle and horizontal lines, respectively. Groups that are significantly different (at $\alpha = 0.05$) are depicted by different colors. The elements cobalt, manganese, nickel, and barium depict some significant differences between some of the analyzed groups.

(Figure 10), with the exception of the hematite artifact of Abel Beth Maacah (ABM) and one from Tel Rehov (HEM1 and HEM2), which appear closer to the Ajlun and Zvar Habaqbuq ores, and two other samples HEM6 and HEM8, which appear closer to the Ajlun ores.

When the Os isotopic ratios of the hematite objects are plotted together with the studied iron deposits (Figure 11), a majority of the objects (9/13) are inconsistent with the studied ores. They generally have lower Os isotopic ratios, certainly with respect to the hydrothermal ores, suggesting a possible correlation to the sedimentary ores. However, the few hematite objects that portray consistency with specific ores differ in their trace elements composition as shown previously (Figure 10). The lack of consistency between the chemical and isotopic composition of the hematite objects with the studied ores suggests that the former unlikely originated from the ores included in this study.

5. Discussion

Iron-ore sources in the Southern Levant were surveyed and characterized in this study in an attempt to identify ore sources that were possibly used for iron production during the Iron Age and later. This is part of an ongoing study of early iron production in the region, which was one of the earliest to adopt iron for mundane purposes. The aims, as described previously, were two-fold: to identify ores that were suitable for bloomery smelting, that is, rich in iron, and determine whether these can be discerned chemically and/or isotopically from one another. As the potential of Os isotope analysis for determining iron provenance was reported previously (Brauns et al., 2013, 2020; Dillmann et al., 2017; Liss et al., 2020; Schwab et al., 2022), this method was implemented here for this purpose. Several hematite artifacts from the early Iron Age were sampled as well and compared against the studied

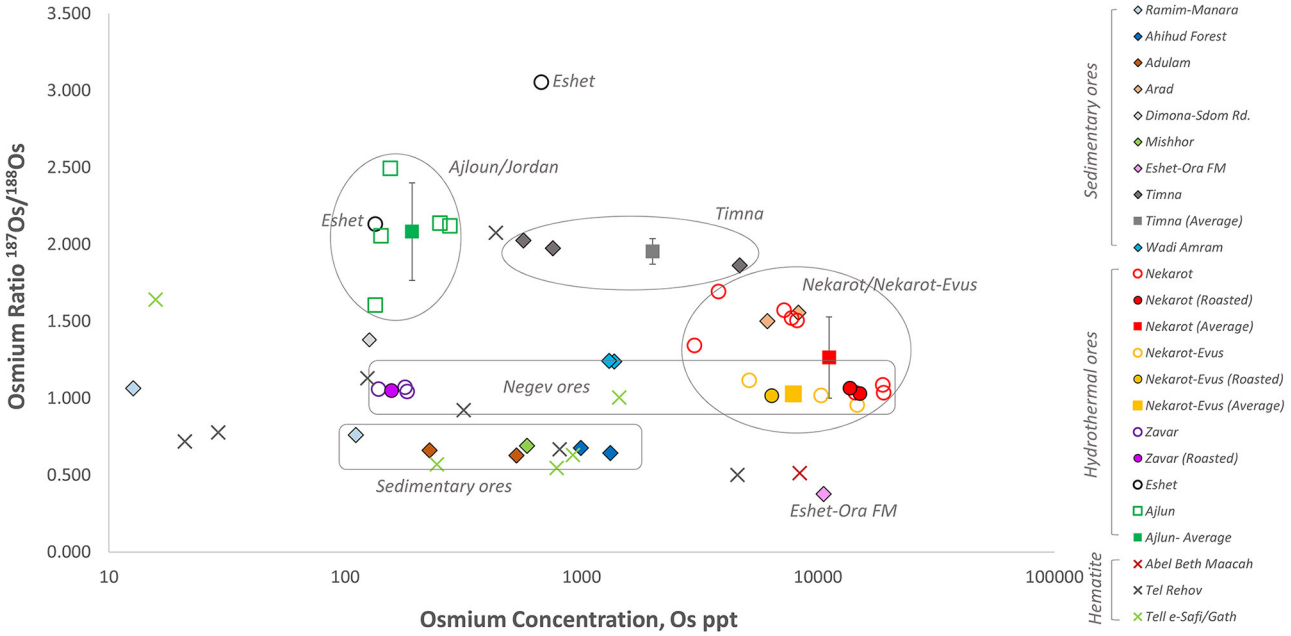

FIGURE 11
$^{187}Os/^{188}Os$ isotopic ratio of the hematite objects analyzed for this study plotted compared to the iron ores shown in Figure 5.

ores in a first attempt to determine whether some of these ores were exploited.

Relying on earlier surveys of iron ores conducted during the 1950s, hydrothermal and sedimentary sources were identified and sampled for analysis. Of the hydrothermal Negev sources, Zvar Habaqbuq is closest to an ancient throughway (at present Route 90) and has the widest surface exposure. No evidence exists to indicate ancient mining there or at any other site in this region. Mugharet el-Wardeh in Ajlun, as mentioned above, is the only source with evidence of exploitation, particularly during the Iron Age. Notably, while some of the hydrothermal sources, particularly Nekarot and Paran in the Negev, and Ajlun in Transjordan, were widely exposed at the surface, sedimentary sources were not. The main results of this preliminary study are discussed next.

5.1. Iron concentrations and suitability for bloomery smelting

In this study, we show that in addition to hydrothermal iron deposits in the Negev and Ajlun that were rich in iron and suitable for bloomery smelting, as expected, some sedimentary ores appear to have been suitable as well.

High iron concentrations in the hydrothermal sources measured in this study reinforced previous analyses (Bender, 1968; Ilani et al., 1985; Erel et al., 2006; Al-Amri, 2008; Ryb, 2008; Ryb et al., 2022), indicating their suitability for bloomery smelting. This was demonstrated by Adi Eliyahu Behar in an experimental procedure, which utilized the Nekarot, Nekarot-Evus, and Zvar Habaqbuq, successfully producing metallic iron (Brauns et al., 2020; Stepanov et al., 2022).

Some of the sedimentary iron sources were richer in iron than previously reported. The Ahihud and Adulam deposits contained iron nodules with a surprisingly high iron concentration reaching up to 70–80 wt% Fe_2O_3. The collection of these nodules may have been time-consuming but not necessarily uneconomical. Moreover, their potentially wide distribution and proximity to major Iron Age urban centers (in particular ʿAkko, Tel Beth Shemesh, and Tell es-Safi/Gath), in which evidence for iron production during the Iron Age was previously reported (Veldhuijzen and Rehren, 2007; Eliyahu-Behar et al., 2012; Killebrew and Quartermaine, 2016; Workman et al., 2020), render the sedimentary ores potential candidates for being sources of iron during the Iron Age. Notably, the iron nodules from Timna, while being quite rich in iron (65 wt% Fe_2O_3), were also relatively enriched with copper (up to 4 wt% CuO), as may be expected in this case. This may not pose a problem for the smelting process, but since these two elements are not miscible, distortions in the iron/steel microstructure occur, thereby compromising the metal's mechanical properties and its workability (e.g., Garza and Van Tyne, 2005; Sekunowo et al., 2014).

5.2. Discerning ore sources

The characterization of the iron ores sampled for this study indicated that despite considerable overlap, there is a possibility of discerning these ores from one another using siderophile elements and Os isotopic composition.

In this study, we were able to generally distinguish between the Ajlun and the Negev deposits using Os isotopic ratios, as well as between different deposits within the Negev, based on Os concentrations. The latter change during smelting, becoming enriched in the final metal product and thus may be useful for

establishing provenance when concentrations in the potential ores are considerably higher and therefore can be eliminated as a possible source for the metal (Brauns et al., 2020).

Notably, the majority of the Negev ores show consistency in their Os isotope ratios (excluding Eshet). When sampled in large quantities for the smelting experiment reported by Brauns et al. (2020), the Os isotopic ratio of the Negev deposits clustered tightly around 1 (see roasted ore isotopic values in Figure 5). The Mugharet el-Wardeh deposit (Ajlun), on the contrary, exhibits relatively high heterogeneity of the Os isotopic ratios. This relative heterogeneity, which does not characterize the other sampled deposits, is also evident in the trace element composition as shown by the computational analysis. While this may be due to the limited number of samples analyzed for this study, Al-Amri (2008), who performed a more systematic analysis ($n = 24$) of this deposit, reached a similar conclusion, showing relatively high variability in iron and calcium concentrations (Al-Amri, 2008, p. 49, Figure 9).[1]

With respect to the sedimentary ores, the Adulam and the Ahihud deposits were discerned based on Os isotopic ratios from the hydrothermal sources mentioned previously exhibiting some of the lowest values (Figure 5). The two samples from Ahihud were discerned from the hydrothermal sources also based on their chemical composition, showing higher nickel, cobalt, and copper concentrations (Figure 10). Note that some of the elements are not significantly different at the $\alpha = 0.05$ significance level; however, this is likely related to the limited number of available data for some of the groups, which reduces the strength of the test to identify differences at low α. Being siderophiles, these elements are of particular significance because they have a high affinity to iron. During the smelting process, these would follow the iron rather than partition into the slag and could potentially aid with determining provenance.

In a recent study, Ilani et al. (2020), suggested that the Adulam Formation was utilized as an iron source for the Tel Beth Shemesh Iron Age smithy. This conclusion was based on the comparison of barium concentrations measured in iron objects, notably corroded, to those measured in the Adulam ores. While an exceptionally high barium concentration was measured in the single Adulam ore sample that we sampled for this study, relatively high barium content was measured in other ores as well (e.g., the Negev ores; see Table 4). Moreover, barium is known to precipitate in porous materials (such as corroded metal) and is often used in geochemical studies to identify diagenetic post-depositional processes and is thus not a good proxy for determining provenance and certainly cannot be used as a sole indicator of source (Lambert et al., 1984; Manea-Krichten et al., 1991).

5.3. Hematite objects

Hematite artifacts from Iron Age archaeological sites were also analyzed in the framework of this study, as it was assumed that these may have been brought from the main iron sources of the period and may be thus indicative of these sources. These artifacts, if carved from the studied ores, should have been both chemically and isotopically consistent with them. However, the analysis of the 13 artifacts, which originated in three Iron Age sites, showed chemical and isotopic heterogeneity (in contrast with the relative homogeneity of each of the studied ore sources) and inconsistency with the studied ores. This suggests that these were brought from multiple deposits (or an extremely heterogeneous one or more), which do not appear to have been sampled for this study.

Generally, however, the Os isotopic composition was relatively low for the majority of the objects, for which there are two possible explanations.

The first is that variable sedimentary iron deposits were used for the production of the rather small hematite objects and that these varied sources were not used for systematic iron production. In this case, the two industries (object making and iron smelting) were fully separated, and the source of the hematite objects is not indicative of the deposits used for iron production. Admittedly, hematite was used throughout all periods for the production of small objects (e.g., in the Chalcolithic period, see Bar-Adon, 1961; Al-Amri, 2008); that is, this was not a practice that began with iron use.

The second possibility is that the role of sedimentary ores in iron production was underestimated for the Southern Levant and that these were, in fact, regularly used as sources of iron (as suggested by Ilani et al., 2020 for Tel Beth Shemesh). The use of sedimentary iron ores for iron production in Europe has been identified and studied (Gassmann et al., 2005; Gassmann et al., 2006, 2014; Brauns et al., 2013; Disser et al., 2017). Many of the Os isotopic ratio $^{187}Os/^{188}Os$ measured for the samples of the south Levantine sedimentary iron ores are within the variation range of sedimentary iron ores from southern Germany as presented in Dillmann et al. (2017; Supplementary 2, Figure 7). This requires that Os isotope analysis, when applied to inter-regional trade of iron, will need to be combined with other chemical variables and will rely heavily on archaeological and historical considerations (Dillmann et al., 2017; Stepanov et al., 2023). For the Early Iron Age in Southern Levant, the possibility that iron was imported from Europe is doubtful, since, as mentioned previously, cultures there lingered behind in the adoption of iron technology (see Erb-Satullo, 2019). Aside from Anatolia and the Northern Levant, from which our knowledge is currently limited, Cyprus is the only region where iron was systematically produced already during the late 2nd millennium BCE (e.g., Sherratt, 1994) and could have been used theoretically as an iron source. However, the few Os isotopic results from the gossan, which is the suggested iron source ("ochre and umber"; Kassianidou, 1994, p. 76), are highly radiogenic, higher than most of the ores from the Southern Levant sampled so far (see Liss et al., 2020), and certainly inconsistent with hematite objects discussed previously.

As mentioned previously, our study shows relatively high iron concentrations in nodules trapped in certain sedimentary formations. Clearly, a much wider sampling of such ores is required, especially since the ores sampled for this study do not appear to be the source of the specific hematite objects sampled here. The suggested use of relatively widespread sedimentary ores, as opposed to much rarer but richer and more concentrated hydrothermal ones, has wide implications regarding sociopolitical and economic organization during the Iron Age, particularly with

1 Unfortunately, the trace elements that Al-Amri measured from this deposit are not the same as in our study and thus are not comparable.

regard to control over iron resources. More data are needed before the latter can be discussed. Moreover, further consideration of more distant sources is necessary, certainly more so as the Iron Age progressed, additional regions adopted iron for common use and the Levant came under imperial rule.

Data availability statement

The original contributions presented in the study are included in the article/Supplementary material, further inquiries can be directed to the corresponding authors.

Author contributions

AE-B and NY-M equally and substantially contributed to the conception and design of the project, including the analysis and interpretation of data and writing of the manuscript. AK contributed to the conception of the project. YB performed the statistical analysis and wrote sections of the manuscript. YA was responsible for the geological survey. MB, OS, and OT prepared samples, conducted the analysis, and wrote sections of the manuscript. All authors contributed to the manuscript's revision and read and approved the submitted version.

Funding

The research presented here was mainly funded by the Israel Science Foundation (Grant No. 1047/17 to AE-B) and additional funds granted to NY-M by the Ruth Amiran Fund for Archaeological Research.

Acknowledgments

The authors wish to express their gratitude to Ivan Stepanov for some of the mineralogical analysis conducted in this research. The ores were surveyed and selected for analysis in collaboration with Yigal Erel. The authors are especially grateful to Erel for providing the chemical analysis and laboratory facility and for his guidance and valuable contribution to the interpretation of the results. We wish to thank Aren M. Maeir of Bar-Ilan University for allowing us to sample the hematite objects from Tell es-Safi/Gath, to Amihai Mazar, The Hebrew University of Jerusalem, for the Tel Rehov materials, to Erez Ben-Yosef of Tel Aviv university, for assistance in ore sampling from Timna, and to Uzi Avner of the Arava Dead Sea Science Center for his help collecting ore samples in Wadi Amram.

Conflict of interest

The authors declare that the research was conducted in the absence of any commercial or financial relationships that could be construed as a potential conflict of interest.

Publisher's note

All claims expressed in this article are solely those of the authors and do not necessarily represent those of their affiliated organizations, or those of the publisher, the editors and the reviewers. Any product that may be evaluated in this article, or claim that may be made by its manufacturer, is not guaranteed or endorsed by the publisher.

Supplementary material

The Supplementary Material for this article can be found online at: https://www.frontiersin.org/articles/10.3389/fearc.2023.1221130/full#supplementary-material

References

Aitchison, J. (1982). The statistical analysis of compositional data. *J. R. Stat. Soc.* 44, 139–160. doi: 10.1111/j.2517-6161.1982.tb01195.x

Al-Amri, Y. A. S. (2008). *The Role of the Iron Ore Deposit of Mugharet el-Wardeh/Jordan in the Development of the Use of Iron in Southern Bilad el-Sham (PhD thesis).* Bochum: Bochum University, Germany.

Bar-Adon, P. (1961). Expedition C. *Israel Explor. J.* 11, 25–35.

Bender, F. (1968). *Geologie von Jordanien, Beitrage zur Regionalen Geologie der Erde*. Berlin: Gebrüder Bornträger.

Birck, J. L., Barman, M. R., and Capmas, F. (1997). Re-Os isotopic measurements at the femtomole level in natural samples. *Geostand. Newslett.* 21, 19–27. doi: 10.1111/j.1751-908X.1997.tb00528.x

Blakelock, E., Martinon-Torres, M., Veldhuijzen, H. A., and Young, T. (2009). Slag inclusions in iron objects and the quest for provenance: an experiment and a case study. *J. Archaeol. Sci.* 36, 1745–1757. doi: 10.1016/j.jas.2009.03.032

Brauns, C. M. (2001). A rapid, low-blank technique for the extraction of osmium from geological samples. *Chem. Geol.* 176, 379–384. doi: 10.1016/S0009-2541(00)00371-5

Brauns, C. M., Hergt, J. M., Woodhead, J. D., and Maas, R. (2000). Os isotopes and the origin of the Tasmanian dolerites. *J. Petrol.* 41, 905–918. doi: 10.1093/petrology/41.7.905

Brauns, M., Schwab, R., Gassmann, G., Wieland, G., and Pernicka, E. (2013). Provenance of Iron Age iron in southern Germany: a new approach. *J. Archaeol. Sci.* 40, 841–849. doi: 10.1016/j.jas.2012.08.044

Brauns, M., Yahalom-Mack, N., Stepanov, I., Sauder, L., Keen, J., and Eliyahu-Behar, A. (2020). Osmium isotope analysis as an innovative tool for provenancing ancient iron: a systematic approach. *PLoS ONE* 15, e0229623. doi: 10.1371/journal.pone.0229623

Buchwald, V. F., and Wivel, H. (1998). Slag analysis as a method for the characterization and provenancing of ancient iron objects. *Mater. Characteriz.* 40, 73–96. doi: 10.1016/S1044-5803(97)00105-8

Bunimovitz, S., and Lederman, Z. (2003). Tel Beth-Shemesh, 2001–2003. *IEJ.* 53, 233–237. doi: 10.1179/03344350378795922 6

Bunimovitz, S., and Lederman, Z. (2012). "Iron age iron: from invention to innovation," in *Studies in Mediterranean Archaeology: Fifty Years On,* Webb, J. M., and Frankel, D. (eds.). (Uppsala: Åströms förlag), 103–112.

Dillmann, P., Schwab, R., Bauvais, S., Brauns, M., Disser, A., Leroy, S., et al. (2017). Circulation of iron products in the North-Alpine area during the end of the first Iron Age (6th-5th c. BC): A combination of chemical and isotopic approaches. *J. Archaeol. Sci.* 87, 108–124. doi: 10.1016/j.jas.2017.10.002

Disser, A., Dillmann, P. H., Leroy, M., l'Héritier, M., Bauvais, S., and Fluzin, P. H. (2017). Iron supply for the building of Metz cathedral: new methodological

development for provenance studies and historical considerations. *Archaeometry* 59, 493–510. doi: 10.1111/arcm.12265

Eliyahu-Behar, A. (2023). "Experimental Bloomery iron smelting in the study of iron technology in the Southern Levant," in *And in Length of Days Understanding (Job 12: 12): Essays on Archaeology in the Eastern Mediterranean and Beyond in Honor*, ed T. E. Levy (Cham: Springer International Publishing), 1449–1466.

Eliyahu-Behar, A., and Yahalom-Mack, N. (2018). Reevaluating early iron-working skills in the southern Levant through microstructure analysis. *J. Archaeol. Sci.* 18, 447–462. doi: 10.1016/j.jasrep.2018.01.040

Eliyahu-Behar, A., Yahalom-Mack, N., Gadot, Y., and Finkelstein, I. (2013). Iron smelting and smithing in major urban centers in Israel during the Iron Age. *JAS.* 40, 4319–4330. doi: 10.1016/j.jas.2013.06.009

Eliyahu-Behar, A., Yahalom-Mack, N., Shilstein, S., Zukerman, A., Shafer-Elliott, C., Maeir, A. M., et al. (2012). Iron and bronze production in Iron Age IIA Philistia: new evidence from Tell es-Safi/Gath, Israel. *J. Archaeol. Sci.* 39, 255–267. doi: 10.1016/j.jas.2011.09.002

Erb-Satullo, N. L. (2019). The innovation and adoption of iron in the ancient near east. *J. Archaeol. Res.* 27, 557–607. doi: 10.1007/s10814-019-09129-6

Erb-Satullo, N. L., and Walton, J. T. (2017). Iron and copper production at Iron Age Ashkelon: implications for the organization of Levantine metal production. *J. Archaeol. Sci.* 15, 8–19. doi: 10.1016/j.jasrep.2017.06.006

Erel, Y., Listovsky, N., Matthews, A., Ilani, S., and Avni, Y. (2006). Tracing end-member fluid sources in sub-surface iron mineralization and dolomitization along a proximal fault to the dead sea transform. *Geochim. Cosmochim. Acta* 70, 5552–5570. doi: 10.1016/j.gca.2006.08.019

Finkel, M., Erel, Y., Dor, Y. B., Tirosh, O., Levy, T. E., Najjar, M., et al. (2022). High resolution elemental characterization of prehistoric flint sources in southern Israel: Implications for archaeological provenance studies. *J. Archaeol. Sci.* 43, 103438. doi: 10.1016/j.jasrep.2022.103438

Garza, L. G., and Van Tyne, C. J. (2005). Surface hot-shortness of 1045 forging steel with residual copper. *J. Mater. Proc. Technol.* 159, 169–180. doi: 10.1016/j.jmatprotec.2004.05.004

Gassmann, G., Augstein, M., and Rösch, M. (2014). Archäologisch-naturwissenschaftliche Untersuchungen einer späthallstatt-/frühlatènezeitlichen Siedlung mit Eisenverhüttung bei St. *Johann-Würtingen auf der Schwäbischen Alb. Fundber. Baden-Württemb.* 34, 237–278.

Gassmann, G., Rösch, M., and Wieland, G. (2006). Das Neuenbürger Erzrevier im Nordschwarzwald als Wirtschaftsraum während der Späthallstatt-und Frühlatènezeit. *Germania* 84, 273–306.

Gassmann, G., Yalçin, Ü., and Hauptmann, A. (2005). "Die Archäometallurgischen Materialuntersuchungen zur keltischen Eisenerzverhüttung in Baden-Württemberg. Abbau und Verhüttung von Eisenerzen im Vorland der mittleren Schwäbischen Alb," *in Gassmann, Hauptmann, Hübner, Rutdhardt, Yalçin, Forschungen und Berichte zur Vor- und Frühgeschichte in Baden-Württemberg,* 84–114.

Gottlieb, Y. (2010). The advent of the age of Iron in the Land of Israel: a review and reassessment. *Tel Aviv* 37, 89–110. doi: 10.1179/033443510x12632070179469

Grosz, S., Matthews, A., Ilani, S., Ayalon, A., and Garfunkel, Z. (2006). Iron mineralization and dolomitization in the Paran Fault zone, Israel: implications for low-temperature basinal fluid processes near the Dead Sea Transform. *Geofluids* 6, 137–153. doi: 10.1111/j.1468-8123.2006.00139.x

Hauptmann, A. (ed.). (2007). *The Archaeometallurgy of Copper: Evidence from Faynan, Jordan*. Berlin; Heidelberg: Springer Berlin Heidelberg.

Ilani, S. (1989). Epigenetic metallic mineralization along tectonic elements in Israel. *Isr. Geol. Surv. Rep.* 3, 487–498.

Ilani, S., Kronfeld, J., and Flexer, A. (1985). Iron-rich veins related to structural lineaments, and the search for base metals in Israel. *J. Geochem. Explor.* 24, 197–206. doi: 10.1016/0375-6742(85)90045-7

Ilani, S., Lederman, Z., and Bunimovitz, S. (2020). Iron oxide concretions as raw material for iron IIA iron metallurgy in the southern Levant: new evidence from Tel Beth-Shemesh, Israel. *J. Archaeol. Sci.* 34, 102570. doi: 10.1016/j.jasrep.2020.102570

Kassianidou, V. (1994). *Could Iron Have Been Produced in Cyprus? Report of the Department of Antiquities of Cyprus*, 73–81.

Killebrew, A. E. (2023). Phoenician iron smithing and cult at persian-period Tel Akko. *J. Eastern Mediterr. Archaeol. Heritage Stud.* 135, 11.

Killebrew, A. E., and Quartermaine, J. (2016). "Total Archaeology@ Tel Akko (The 2013 and 2014 Seasons): Excavation, Survey, Community Outreach and New Approaches to Landscape Archaeology in 3D," in *Proceedings of the 9th International Congress on the Archaeology of the Ancient Near East* (*Harrassowitz Wiesbaden)* 491–502. doi: 10.2307/j.ctvc76zz7.39

Kruskal, W. H., and Wallis, W. A. (1952). Use of ranks in one-criterion variance analysis. *J. Am. Statist. Assoc.* 47, 583–621. doi: 10.1080/01621459.1952.10483441

Lambert, J. B., Simpson, S. V., Szpunar, C. B., and Buikstra, J. E. (1984). Copper and barium as dietary discriminants: the effects of diagenesis. *Archaeometry* 26, 131–138. doi: 10.1111/j.1475-4754.1984.tb00328.x

Liss, B., Levy, T. E., and Day, J. M. D. (2020). Origin of iron production in the Eastern Mediterranean: osmium isotope and highly siderophile element evidence from Iron Age Jordan. *J. Archaeol. Sci.* 122, 105227. doi: 10.1016/j.jas.2020.105227

Manea-Krichten, M., Patterson, C., Miller, G., Settle, D., and Erel, Y. (1991). Comparative increases of lead and barium with age in human tooth enamel, rib and ulna. *Sci. Total Environ.* 107, 179–203. doi: 10.1016/0048-9697(91)90259-H

McNutt, P. M. (1990). *The Forging of Israel: Iron Technology, Symbolism and Tradition in Ancient Society*. Sheffield: Bloomsbury.

Piper, D. Z., and Bau, M. (2013). Normalized rare earth elements in water, sediments, and wine: identifying sources and environmental redox conditions. *Am. J. Analyt. Chem.* 4, 15. doi: 10.4236/ajac.2013.410A1009

Ryb, U. (2008). *Epigenetic Mineralization Phenomena Along the Northern Negev Anticlines and Their Geochemical Anomalies*. Jerusalem: Hebrew University of Jerusalem.

Ryb, U., Erel, Y., Matthews, A., Avni, Y., and Stern, D. (2022). Sources, timing, environmental and tectonic implications of epigenetic mineralization along the Arabian-African plate boundary. *Geochem. Geophys. Geosyst.* 23, e2022GC010549. doi: 10.1029/2022GC010549

Schwab, R., Brauns, M., Fasnacht, W., Katzev, S. W., Lockhoff, N., and Swiny, H. W. (2022). From Cyprus, or to Cyprus? A pilot study with osmium isotopy and siderophile trace elements to reconstruct the origin of corroded iron billets from the Kyrenia shipwreck. *J. Archaeol. Sci.* 42, 103365. doi: 10.1016/j.jasrep.2022.103365

Schwab, R., Heger, D., Höppner, B., and Pernicka, E. (2006). The provenance of iron artefacts from Manching: a multi-technique approach. *Archaeometry* 48, 433–452. doi: 10.1111/j.1475-4754.2006.00265.x

Sekunowo, O. I., Durowaye, S. I., and Gbenebor, O. P. (2014). Effect of copper on microstructure and mechanical properties of construction steel. *Int. J. Chem. Molec. Nucl. Mater. Metallur. Eng.* 8, 839–843.

Sherratt, S. (1994). "Commerce, iron and ideology: metallurgical innovation in 12th−11th century Cyprus," in *Cyprus in the 11th Century BC* (Nicosia, Cyprus: AG Leventis Foundation) 59–107.

Šidák, Z. (1967). Rectangular confidence regions for the means of multivariate normal distributions. *J. Am. Statist. Assoc.* 62, 626–633. doi: 10.1080/01621459.1967.10482935

Stepanov, I., Avner, U., Brauns, M., Lockhoff, N., and Eliyahu-Behar, A. (2023). Nabataean iron picks for copper mining from Nahal 'Amram, Israel; Chemical, isotopic and production technology analysis. *J. Archaeol. Sci.* 51, 104166. doi: 10.1016/j.jasrep.2023.104166

Stepanov, I., Borodianskiy, K., and Eliyahu-Behar, A. (2020). Assessing the quality of iron ores for bloomery smelting: laboratory experiments. *Minerals* 10, 33. doi: 10.3390/min10010033

Stepanov, I. S., Sauder, L., Keen, J., Workman, V., and Eliyahu-Behar, A. (2022). By the hand of the *smelter:* tracing the impact of decision making in bloomery iron smelting. *J. Archaeol. Anthropol. Sci.* 14, 80. doi: 10.1007/s12520-022-01516-3

Tylecote, R. F. (1992). *A History of Metallurgy*. London: Inst. Material.

Veldhuijzen, H. A., and Rehren, T. (2007). "Slags and the city: early iron production at Tell Hammeh, Jordan, and Tel Beth-Shemesh, Israel," in *Metals and Mines: Studies in Archaeometallurgy, eds.* S., La Niece, D.R., Hook, P.T., Craddock (London: JSTOR), 189–201.

Veldhuijzen, X., and van der Steen, E. (1999). Iron production center found in the Jordan Valley. *Near Eastern Archaeol.* 62, 195–199. doi: 10.2307/3210714

Waldbaum, J. C. (1978). *From Bronze to Iron: The Transition from the Bronze Age to the Iron Age in the Eastern Mediterranean, Studies in Mediterranean archaeology*. Göeteborg: Paul Åström.

Waldbaum, J. C. (1999). The coming of iron in the Eastern Mediterranean: thirty years of archaeological and technological research. *MASCA Res. Papers Sci. Archaeol.* 16, 27–57.

Workman, V., Maeir, A. M., Dagan, A., Regev, J., Boaretto, E., and Eliyahu-Behar, A. (2020). An iron IIA iron and bronze workshop in the lower City of tell es-safi/gath. *Tel Aviv* 47, 208–236. doi: 10.1080/03344355.2020.1820040

Yahalom-Mack, N., and Eliyahu-Behar, A. (2015). The transition from bronze to iron in Canaan: chronology, technology, and context. *Radiocarbon* 57, 285–305. doi: 10.2458/azu_rc.57.18563

Yahalom-Mack, N., Eliyahu-Behar, A., Kleiman, A., Shahack-Gross, R., Homsher, R. D., Gadot, Y., et al. (2017). Metalworking at megiddo during the late bronze and iron ages. *JNES.* 76, 53–74. doi: 10.1086/690635

Yahalom-Mack, N., and Rabinovich, A. (2020). "Metal Objects," in *Tel Reḥov, A Bronze and Iron Age City in the Beth -Shean Valley* (Jerusalem: The Institute of Archaeology, The Hebrew University of Jerusalem), 133–173.